Next generation of integrated sea ice information services for the Polar Regions

Grant agreement number: 606935

Deliverables: D4.2, D5.2, D6.2, D7.2

Integrated Product Specification Report

Name of the coordinating person:
Nick Walker, eOsphere Limited

THEME (SPA.2013.1.1-06)
Stimulating development of downstream services and service evolution
POLAR ICE is supported by the European Union's Seventh Framework Programme (FP7). All opinions expressed are the author's.

Table of Contents

1 Document details

1.1 Document Information

WP Numbers	WP4, WP5, WP6, WP7
WP Titles	Sea ice pressure, Sea ice thickness, Sea-ice forecasts, Transition to Sentinel
Document	Integrated Product Specification Report
Revision:	V1.0
Date	28/12/2014
Main Authors	WP4, WP5, WP6, WP7 project partners
Main Author Institutions	WP4, WP5, WP6, WP7 project partners
Main Author emails	nick.walker@eosphere.co.uk
Contributors	WP4, WP5, WP6, WP7 project partners
Security	RE = Restricted to a group specified by the consortium (including the Commission Services)

1.2 Distribution

POLAR ICE Consortium, European Commission

1.3 Document history

Version	Date	Comments & Status	Author
V1.0	28/12/2014	First version	Nick Walker (editor)

1.4 Reference Documents

- Grant agreement no: 606935, Annex I - "Description of Work".
- "Part B" of a proposal in response to: Work Programme 2013, Cooperation, Theme 9, Space (European Commission C (2012) 4536 of 09 July 2012).

1.5 POLAR ICE Consortium and contacts

Participant no.	Participant organisation name	Country
1 (Coordinator)	**eOsphere Limited**	**UK**
Contact(s):	Nick Walker	
2	**NERC - British Antarctic Survey (BAS)**	**UK**
Contact(s):	Andrew Fleming. Andreas Cziferszky	
3	**Danish Meteorological Institute (DMI)**	**Denmark**
Contact(s):	Leif Pedersen	
4	**Polar View Earth Observation Limited**	**UK**
Contact(s):	Nick Walker, Dominic Flach	
5	**Finnish Meteorological Institute (FMI)**	**Finland**
Contact(s):	Marko Mäkynen, Eero Rinne	
6	**Technical Research Centre of Finland (VTT)**	**Finland**
Contact(s):	Robin Berglund, Seitsonen Lauri, Tergujeff Renne	
7	**Norsk Regnesentral - Norwegian Computing Center (NR)**	**Norway**
Contact(s):	Oystein Rudjord, Rune Solberg	
8	**Norwegian Meteorological Institute (MetNo)**	**Norway**
Contact(s):	Helge Tangen, Gunnar Noer	
9	**Swedish Meteorological and Hydrological Institute (SMHI)**	**Sweden**
Contact(s):	Anette Jönsson, Robert Olsson, Lake Iréne, Markus Meier, Lars Axell	
10	**Technical University of Denmark (TUD)**	**Denmark**
Contact(s):	Roberto Saldo, Henning Skriver	
11	**Univesitaet Bremen - University of Bremen**	**Germany**
Contact(s):	Christian Melsheimer, Georg Heygster	
12	**Kongsberg Satellite Services (KSAT)**	**Norway**
Contact(s):	Stein Støver, Hans Larsen	
13	**C-Core**	**Canada**
Contact(s):	Thomas Puestow	
14	**Hickling Arthurs Low (HAL)**	**Canada**
Contact(s):	David Arthurs	

2 POLAR ICE Documents Overview

The POLAR ICE project has four main components as illustrated schematically in Figure 1. The following bullet points explain how these four components are mapped onto the project's deliverable documents.

- **New products:** A series of advanced sea-ice information products are being developed as a part of the project. This "**Product Specification**" document provides a detailed description of these products, including their basic algorithms, their output formats and validation to-date.
- **User engagement:** Demonstrating the project's products and systems with end users operating in polar regions is a key component of the project. The results of consultations with 22 end users were described in the "**Requirements and Gap Analysis**" document, covering sectors including: oil & gas, fishing, science, coast guard, ice service, fisheries regulator, oil spill, tourism, icebergs, SAR, meteo and icebreaking. The plan for demonstrating the project's products and systems with selected end users is described in the "**Demonstration Plan**" document.
- **Integration, delivery & visualisation:** One of the main current gaps in the provision of sea ice services to operators in polar waters is the efficient delivery of integrated services which can be visualised readily by end users. Two of the project's WPs are devoted to providing systems which will integrate and deliver all of the project's products and to visualise these both for onshore and offshore users. The systems will also accommodate data from a wide range of other sources, in particular meteorological data, allowing end users to benefit from synergy from many information sources. The "**Software Design document**" provides both a high level and a detailed description of the integration, delivery & visualisation software.
- **Business case analysis:** A business case is being developed so that the POLAR ICE project can transition to sustainable services into the future. A "**Cost benefit analysis & business case**" document will be delivered at the end of the project.

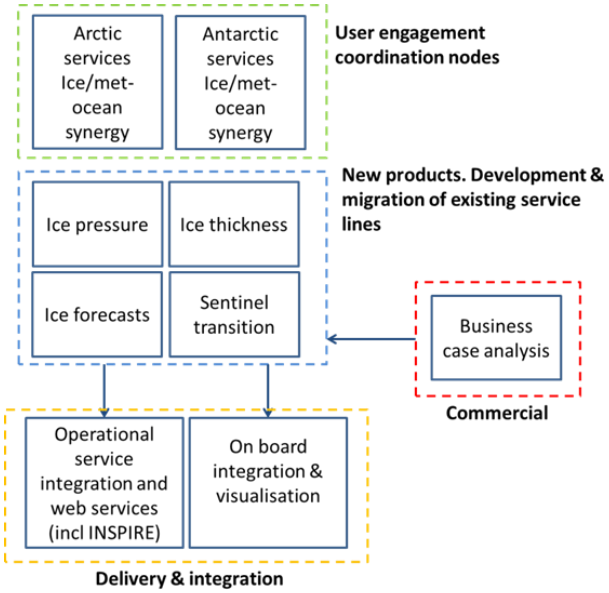

Figure 1. The four main components of the POLAR ICE project.

3 WP4 - Sea Ice Pressure

3.1 Overview

Ice pressure is an important parameter for successful navigation through pack ice as well as for supporting off-shore platforms operations. High ice pressure not only reduces the manoeuvrability of ships but also increases the risk of ships and fixed platforms being damaged. Ice pressure is caused by convergence in the ice drift field and is also related to the ice thickness. Ice convergence is caused by a variety of factors including ocean currents and wind drift.

Ice pressure is difficult to retrieve simply by observing the current state of the ice, but instead requires very accurate ice drift and ice thickness information. With the advent of Synthetic Aperture Radar (and especially Sentinel-1 SAR) more accurate ice drift data has become available and can be used to infer ice pressure information.

The Canadian Coast Guard manual on Navigation in ice covered waters states:

> *The easiest way to avoid being beset is to avoid areas of ice under pressure. Ice can be put under pressure in several ways. The most common pressure situation occurs when open pack ice closes because of prevailing winds, but it may also occur when tides, currents, or on-shore breezes blow ice onto the shore.*
>
> *The danger from becoming beset is increased greatly in the presence of old or glacial ice, as the pressure on the hull is that much greater. When in pack ice, a frequent check should be made for any signs of the track closing behind the ship. Normally there will be a slight closing from the release of pressure as the ship passes through the ice, but if the ice begins to close up completely behind the ship it is a strong sign that the pressure is increasing. Similarly, if proceeding along an open water lead between ice and shore, or ice in motion and fast ice, watch for a change in the wind direction or tide as the lead can close quickly.*
>
> *Pack ice that has been under pressure for some time will deform, overriding as rafts or piling up as ridges or hummocks. Appearances are deceiving as the sail on a ridge or hummock may be only 1 to 2 metres above the ice cover but the keel could be several metres below.*

And they go on saying:

> *Planning may be as for open water on large-scale charts, but also, if further information has been obtained, this may involve a track planned on a small-scale chart. Planning with additional information entails laying off the route to take the best advantage of optimum ice conditions, including:*
>
> - *finding open water leads;*
> - *finding first-year ice leads in close ice or old ice fields;*
> - *avoiding areas of ridging; and*
> - *avoiding areas of pressure or potential pressure.*
>
> *Once the track has been laid out, it has to be transferred to large-scale charts and checked for adequate water depth. The two sources have to be reconciled so that the best route is also a safe route. Once the route has been laid out it may indicate the need for further information.*

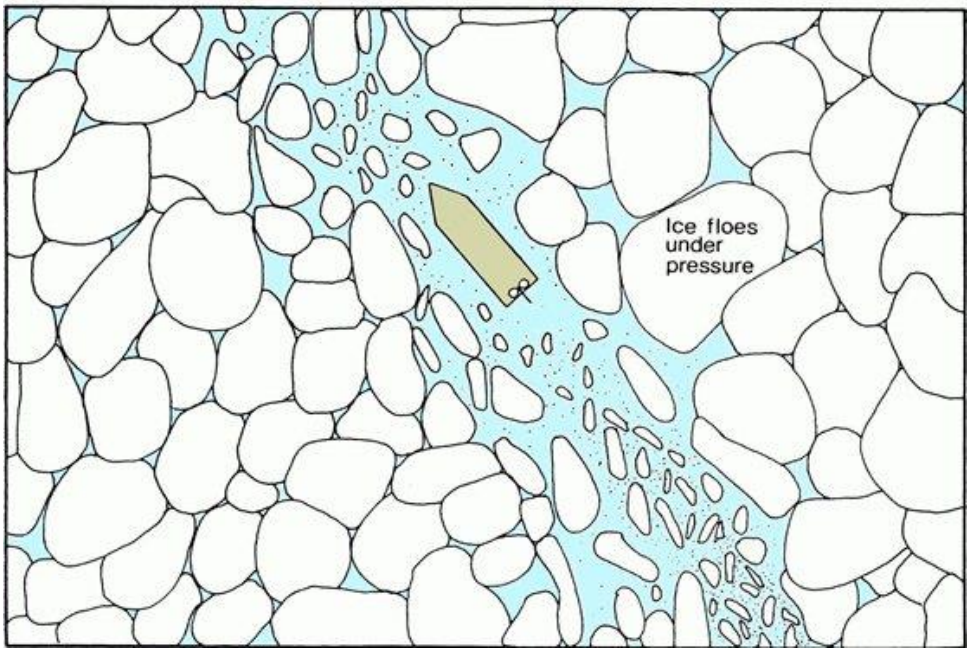

Figure 2. Pressure in ice field closes track behind vessel (From http://www.ccg-gcc.gc.ca/Icebreaking/Ice-Navigation-Canadian-Waters/Navigation-in-ice-covered-waters)

As a part of the POLAR ICE project the following issues will be addressed:

- Sea ice deformation fields derived from ice drift observations using satellite data:
  - Areas of divergence (openings)
  - Areas of Convergence (pressure)
- Sea ice pressure indicators computed from deformation fields

3.2 Algorithm description

Ice divergence information is generated from high-resolution (10 Km) 1-day ice drift data produced by the Copernicus Marine Core Service (MyOcean[1]).

Input data needed are daily Synthetic Aperture Radar data from Sentinel-1 or similar instruments. Extended Wide Swath mode (EWS) is normally used, but Interferometric Wide Swath mode (IWS) data can also be used. EWS data are normally delivered to the Copernicus Marine Core Service on a 40 m grid at a resolution of approximately 90m (medium resolution product). Alternative data sources are Radarsat-2 ScanSAR Wide (SCW) and from the past also RADARSAT-1 SCW and ENVISAT WSM images have been used.

[1] The MyOcean (2009-2012) , MyOcean2 (2012-2014) and MyOcean follow-on (October 2014- March 2015) projects, respectively funded by the EU's Seventh Framework Programme for Research (FP7 2007-2013) and HORIZON 2020 (EU Research and Innovation programme 2014-2020) have been designed to prepare and to lead the demonstration phases of the future Copernicus Marine Environment Monitoring Service. The latter is meant to be full operational from 2015 onwards. http://www.myocean.eu/

The Mathematical definition of the divergence of a vector field is:

$$\mathrm{Div}(V) = \frac{\partial V_x}{\partial x} + \frac{\partial V_y}{\partial y}$$

which in terms of the area spanned by 4 ice drift vectors at time=0 and time=1 is

$$\mathrm{Div}(\mathbf{V}(\mathbf{x},\mathbf{y})) = \frac{\text{rate of change of area of span}}{\text{area of span}}$$

Figure 3 below illustrates the processing steps involved in producing the ice pressure (divergence/convergence) product.

1. Collect Sentinel-1 and/or Radarsat-2 SAR data from near real time data provider (MDA, KSAT, ESA).
2. Geometric processing of the SAR scenes into a common reference coordinate system, including some speckle noise reduction. The coordinate system used here is a Polar Stereographic projection to enable applications throughout the polar regions.
3. All pairs of SAR scenes on consecutive dates covering overlapping areas are processed into an ice drift product using a 10 kilometer diameter circular reference area and a 30 kilometer search area. Ice drift vectors are derived on a regular 10 km grid. Ice drift is archived as start (lat/lon) of an ice drift vector and end (lat/lon) of an ice drift vector directly.
4. Four ice drift vectors are combined to produce an estimate of convergence/divergence. The area of the polygon spanned by the 4 start points of the ice drift vectors is computed, as is the area spanned by the 4 end-points. Relative changes in the area are subsequently stored as an indication of the ice pressure at the center location of the 4 end points.

The MyOcean ice drift vectors are available throughout the year, and the ice divergence/ convergence can be provided at all seasons.

The ice drift data are sparser in the marginal ice zone[2] (MIZ) where the ice features are comparable to or smaller than the resolution of the data, and rapidly changing. This means that the method seldom will provide ice deformations in the MIZ (when the ice concentration is less than 90%, convergence is not necessarily an indication of ice pressure).

It is planned to include shear deformation rate (SDR) as an additional deformation parameter in the future, given by:

$$SDR(V(x,y) = \frac{\delta V_y}{\delta x} + \frac{\delta V_x}{\delta y}$$

[2] The marginal ice zone is commonly described as that part of the ice cover which is close enough to the open ocean boundary to be affected by its presence, which makes it an area of enhanced ice drift, deformation and divergence.

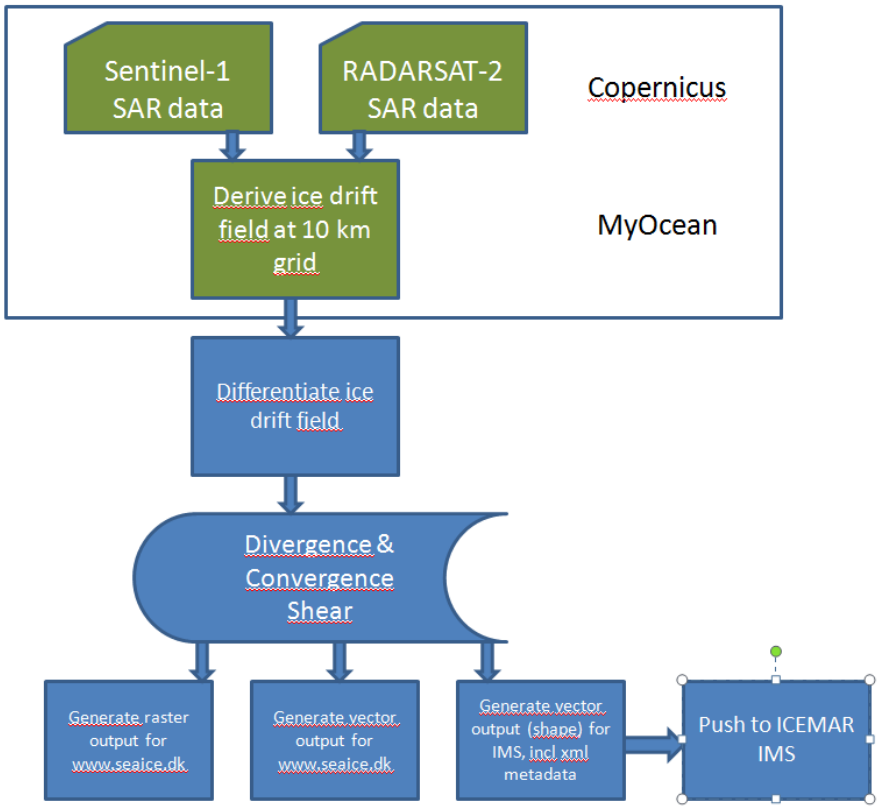

Figure 3. Block diagram illustrating the processing steps involved in generation of the derivation of ice divergence/convergence from daily Sentinel-1 or RadarSAT SAR data, and the dissemination of the products to the POLAR ICE distribution sites (www.seaice.dk and IMS).

3.3 Output formats

The output convergence/divergence products are generated in raster as well as vector format. Format of the raster data are Geotiff, format of the vector data is ESRI shape.

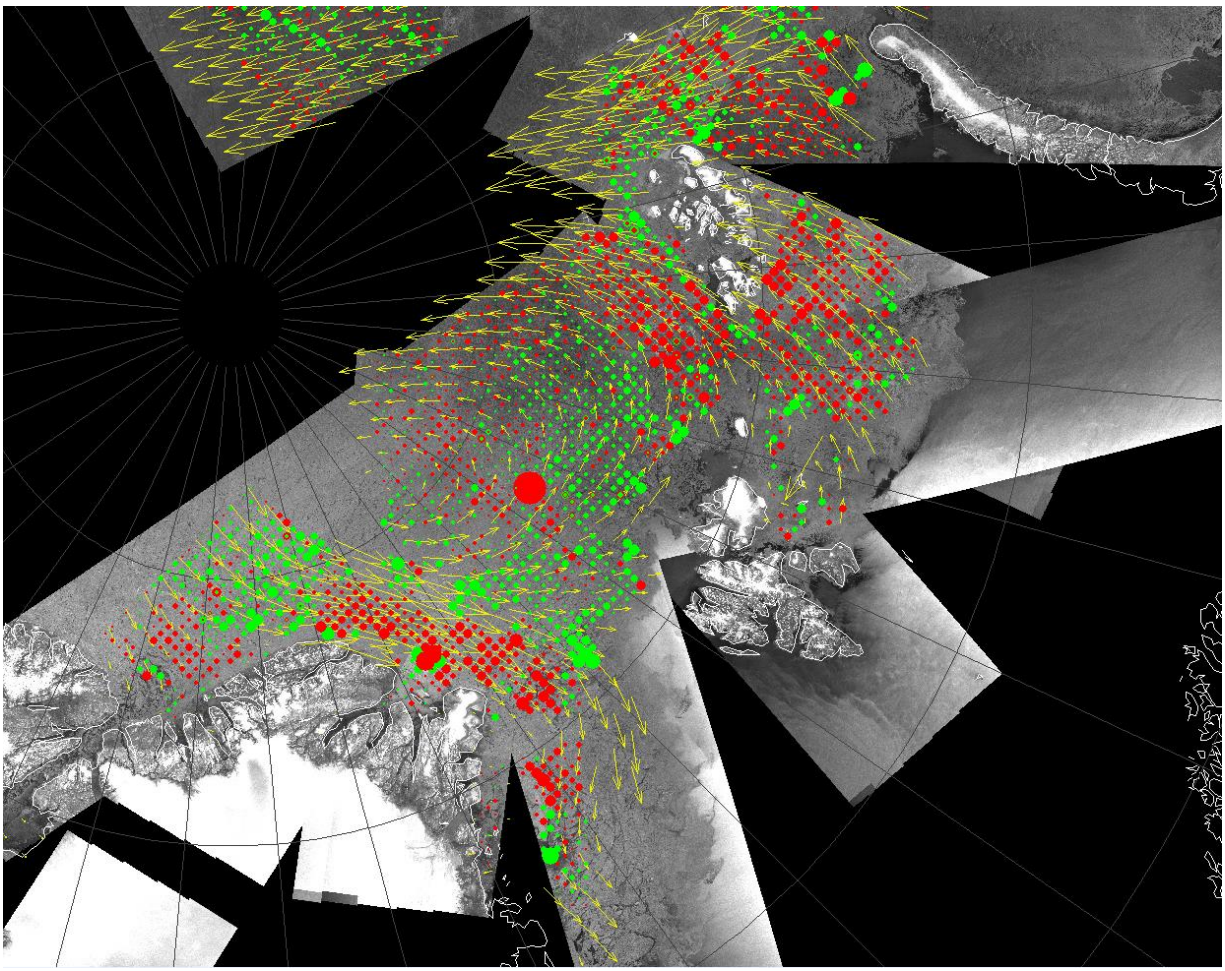

Figure 4. Example of ice divergence/convergence computed from MyOcean ice drift data between November 27 and 28, 2014. Red areas are areas of convergence (indication of ice pressure) and green areas are areas of divergence (low ice pressure). Area north of Fram Strait where ice pressure often is a problem to navigation. The example illustrates a rendition of the ice pressure data in vector form overlaid on a Sentinel-1 image mosaic.

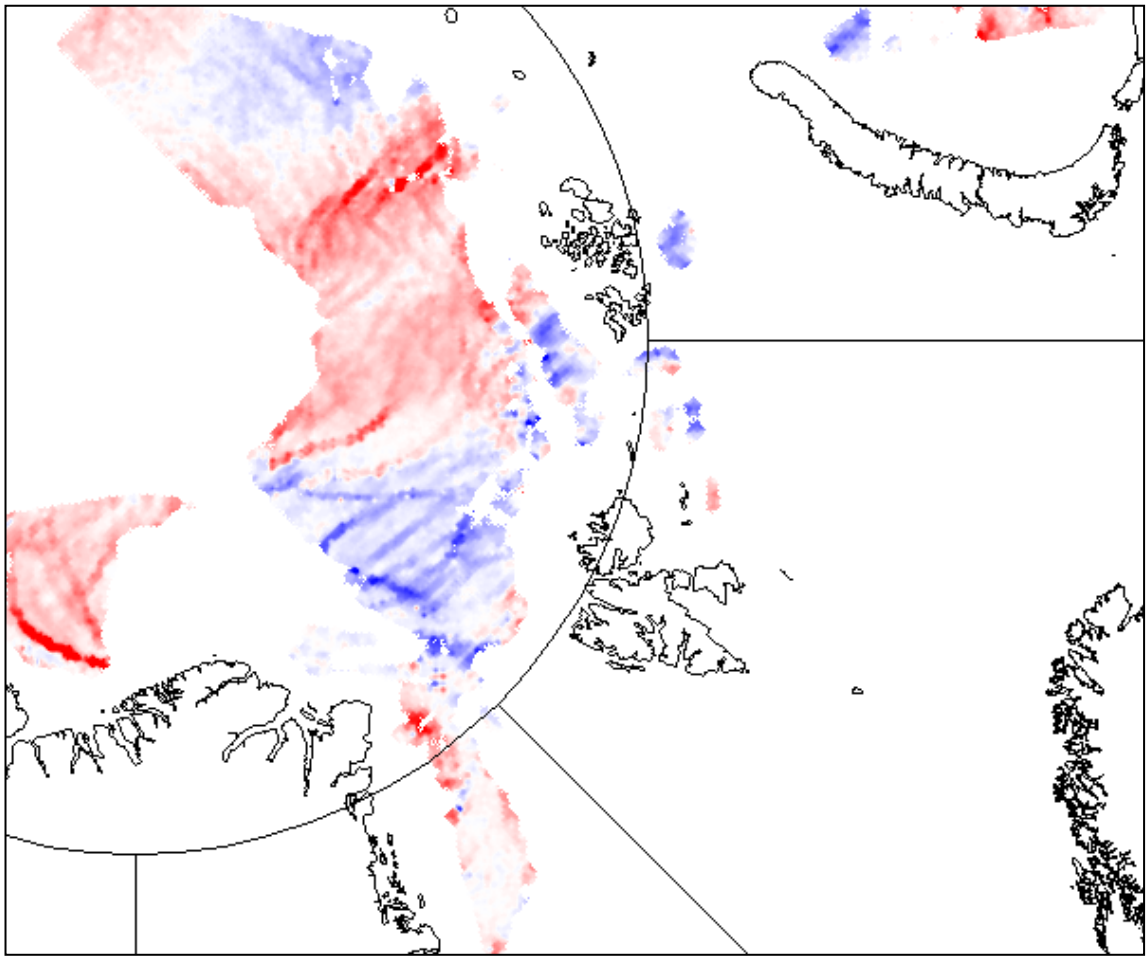

Figure 5. Example of ice divergence/convergence map in raster format. Blue areas are areas of divergence (little ice pressure), red areas are areas of convergence (ice pressure). Data are generated from ENVISAT SAR data in January 9 and 10, 2010.

3.4 Validation

Ice drift data have been validated using GPS buoys with a sampling of location every hour. Correspondence between buoy drift and satellite derived drift is excellent. Root men squared (RMS) differences are in the order of 300 m in 24 hours. The differences that do exist may be due to uncertainties in the satellite ice drift, but may also be due to the discrepancy of buoy (single point) data to represent the drift of a 10 km area as observed by the satellite.

Figure 6 and Figure 7 show results of validation of MyOcean ice drift observations from SAR satellite data using GPS buoy drift as reference.

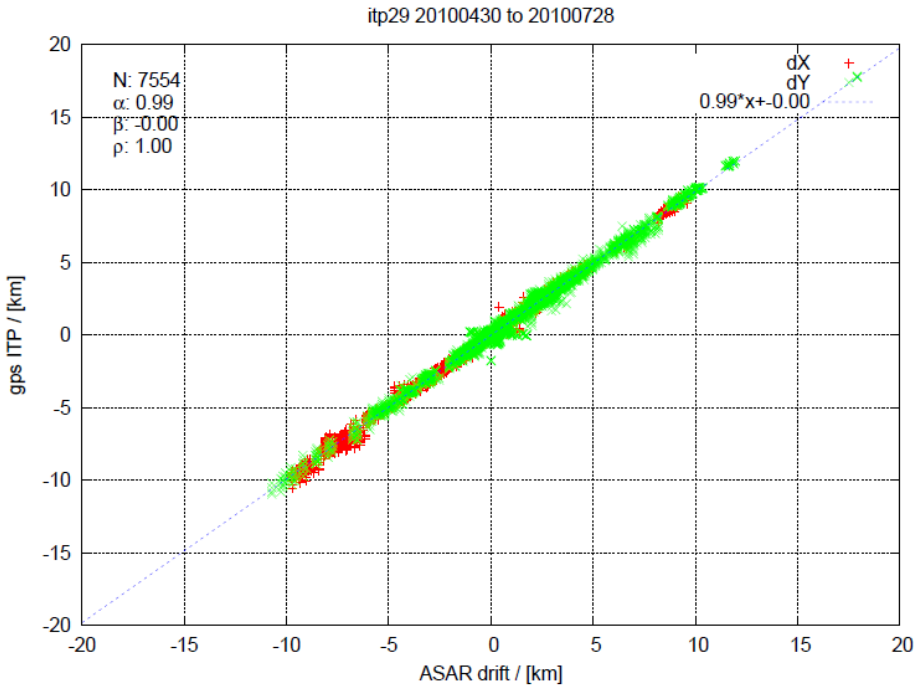

Figure 6. Scatter plot of buoy drift versus SAR derived ice drift.

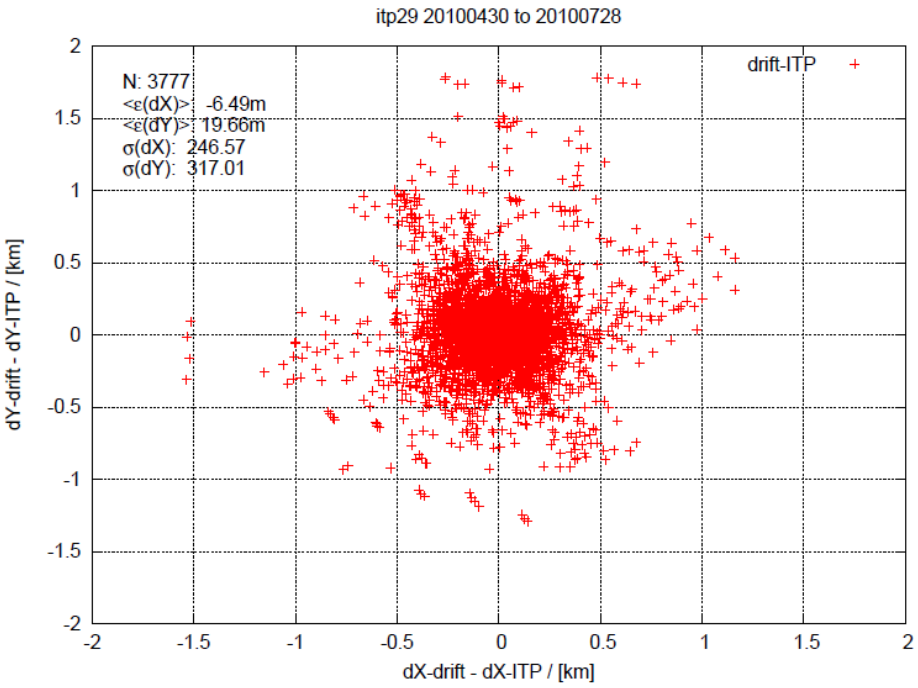

Figure 7. Scatterplot of difference between buoy drift and satellite derived ice drift. RMS difference is approximately 250 m in x direction and 317 m in y direction.

Based on the ice drift validation results it is considered that area changes in the order of 2-3% can be reliably derived from the satellite ice drift data. Convergence/divergence less than 2-3% are thus considered insignificantly different from 0%.

More thorough validation will require arrays of buoys at an array grid spacing of approx. 10 km. This is planned to be conducted in collaboration with FP7 project ICE-ARC.

3.5 Product summary

Ice pressure data are delivered at a 10 km and a 20 km grid spacing, given as % change in area of a regular grid laid out at fixed locations on the ice. As the ice moves, the area changes, and reduction in areas (convergence) is indicated as ice pressure, and an expansion of area (divergence) is indicated as no ice pressure.

Since this is an experimental product, user experience will be collected during the demo phases.

Table 1. Summary of properties of the DMI sea ice pressure product.

Product description	Maps of ice convergence and divergence as an indicator of ice pressure during the past 24 hours.
Satellite input data	Sentinel-1 and Radarsat-2 SAR data on 2 consecutive days
Model input data	None
Sea ice parameter(s)	Convergence and divergence
Coverage	Area north of Fram Strait, North East Greenland and Baffin Bay Other areas less frequently
Update interval	Every day in most of the area, depending on the SAR image coverage
Spatial resolution	10 km and 20 km
Delivery time	<6 h after aquisition of 2nd image of the area
Formats	GeoTIFF-image, shape file

4 WP5 - Sea ice thickness

4.1 Sea ice thickness overview

Currently Arctic and Antarctic sea ice thickness information is operationally available mainly as WMO ice type classification in ice charts provided by national Ice Services and as estimates by various ocean-sea ice models (e.g. MyOcean TOPAZ). POLAR ICE will distribute in 2015-2016 three new sea ice thickness products based on satellite data for operational usage:

1. SMOS-based thin ice thickness charts for the Arctic and Antarctic (Univ. Bremen). The thickness chart has grid cell size 12.5 km, and spatial resolution of 30-40 km.
2. VIIRS thermal-imagery-based thin ice thickness charts for the Arctic and Antarctic (Norwegian Computing Center). The chart has a spatial resolution of 750 m. The calculation of the ice thickness requires cloud-free conditions.
3. Multisensor (AMSR2 radiometer, SMOS thin ice thickness chart, RADARSAT-2 or SENTINEL-1 SAR) and TOPAZ ocean-sea ice model based thickness chart for the Barents and Kara Seas (Finnish Meteorological Institute). The chart has spatial resolution of 1 km and shows estimated thickness for first-year sea ice up to 2.5 m.

Satellite data based sea ice thickness estimation is possible only in cold winter conditions (dry snow cover), e.g. in the Arctic from Sep/Oct to April/May. The SMOS and VIIRS thin ice thickness charts are issued daily and the multi-sensor thickness chart every 1-3 days depending on satellite data coverage. The thickness products will be available as GeoTIFF-images (numerical data for POLAR ICE visualisation software) and map-images (for any image viewing software; format does not include detailed geographic information). The data volume of these images is small enough for quick and low-cost download through low-capacity satellite links.

POLAR ICE ice thickness products will improve the safety and efficiency of shipping, fisheries, tourism and off-shore operations in Arctic and Antarctic waters. For these end-users, the products will allow improved decision making at both short time scales (e.g. real time navigation) and medium to long term planning (route planning and risk assessment). The improved accuracy and quality of the sea ice thickness products will provide accurate and reliable input for Ice and Weather Services and climate modelling. POLAR ICE ice thickness observations will also feed into the engineering design of ships and off-shore platforms.

In Section 4.2 guidelines for end-users for selecting which ice thickness chart(s) to use are given. In Sections 4.3 to 4.5 the three POLAR ICE sea ice thickness products are described in detail.

4.2 Guidelines for end-users to select a sea ice thickness product

The main properties of the three ice thickness products are summarized in Table 2. The following points provide guidelines for end-users for selecting which thickness chart or charts to use:

- Interested on overview of location of thin ice and its thickness estimations in the whole Arctic or Antarctic?
  - ⇒ SMOS thin ice thickness chart: 12.5 km grid cell (pixel) size, full daily Arctic and Antarctic coverage.
  - ⇒ VIIRS thin ice thickness chart: 750 m pixel size, daily spatial coverage typically limited by clouds, but on cloud-free areas gives sea ice thickness information in much finer spatial resolution (750 m) than the SMOS thickness chart (12.5 km).
- Interested on location of ice edge and thin ice areas in the Greenland and Barents Seas; typical end-user is fishing industry?
  - ⇒ VIIRS thin ice thickness chart.
  - ⇒ SMOS thickness chart as back-up if an area of interest is cloudy in the VIIRS chart.
- Ship navigation and off-shore operations in the Barents and Kara Seas?
  - ⇒ Multisensor and TOPAZ sea ice model-based thickness chart: 1 km pixel size.
  - ⇒ SMOS thickness chart as back-up if new chart has not been released due to poor SAR image coverage.
- Ice charting?
  - ⇒ All three products can be used as input data.
- Assimilation of sea ice information to an ocean-sea ice model or numerical weather forecasting model?
  - ⇒ SMOS thickness chart: always daily coverage over an area of interest.

Table 2. Main properties of the three POLAR ICE thickness charts.

	SMOS thin ice thickness chart	VIIRS thin ice thickness chart	Multi-sensor data and Topaz model based thickness chart
Producer	Univ. Bremen	NR	FMI
Coverage	Arctic and Antarctic	Arctic Barents and Greenland Seas	Barents and Kara Seas
Spatial resolution	12.5 km	750 m	1 km
Ice thickness range	0-50 cm thick ice (>50 cm)	0-100 cm	0-250 cm
Satellite data used	SMOS L-band radiometer	VIIRS spectrometer thermal imagery	AMSR2 radiometer, RADARSAT-2 or SENTINEL-1 SAR
Update interval	Daily	Daily	Every 1-3 days depending on SAR image coverage
File formats	Map image GeoTIFF	Map image GeoTIFF	Map image GeoTIFF
Notes	Full Arctic and Antarctic coverage every day	Daily coverage depends on clouds	-

4.3 FMI Sea ice thickness product

4.3.1 Overview

For the Barents and Kara Seas only coarse resolution (~10-20 km) satellite data based sea ice products (e.g. sea ice concentration) are now operationally available (e.g. MyOcean products) in addition to the Russian and Norwegian sea ice charts. The ice information available is not accurate enough for various off-shore and shipping operations.

In recent years FMI has been developing a sea ice thickness chart (ITC) based on multi-sensor satellite data and modelled ice thickness (Similä et al 2013). The first operational version of ITC was demonstrated in ESA funded ANISTIAMO project (Addressing new challenges in satellite based maritime surveillance and Arctic monitoring) running from 2012 to 2014. The demonstration period was Jan-Apr 2014.

Multi-sensor sensor data now used in the ITC production include RADARSAT-2 ScanSAR dual-polarised images and AMSR2 radiometer 36 and 89 GHz brightness temperature (T_B) data. The modelled ice thickness field comes from the MyOcean TOPAZ-4 coupled ocean-sea ice data assimilation system (Sakov et al. 2012). Thin ice areas are detected using AMSR2 data and Topaz ice thickness field (thin ice areas missed by the AMSR2 data). The maximum thickness of detected thin

ice is estimated to be 30 cm corresponding maximum thickness of WMO young ice type. It is noted that AMSR2 data may assign thin ice class to areas which according to the Topaz model are thicker ice. We consider identification of thin ice areas with the AMSR 2 data (empirical method (Mäkynen and Similä 2014)) more reliable than using the Topaz, or any other, model data. For thicker ice areas SAR data are used to modulate locally the TOPAZ ice thickness field. The exclusion of thin ice areas reduces significantly the ambiguity of the radar backscatter in the SAR images. The average thickness corresponding to a SAR backscatter level is derived using the TOPAZ ice thickness field and the equivalent deformed ice thickness. Open water and areas with sea ice concentration (SIC) less than 70% are identified using the AMSR2 based SIC data provided by JAXA and excluded from the ice thickness estimation. The spatial resolution of the thickness chart is 1 km. The ice thickness retrieval works under cold wintertime conditions, typically from early November to April/May. Under summer melting conditions the ice thickness estimation is not possible with the adopted method. The ITC area in shown in Figure 8 and an example ITC in Figure 9. More charts for the winter 2014 are available on the ANISTIAMO web-site: http://www.arcice.org.

In the POLAR ICE version of the ITC the SMOS thin ice thickness chart will be used to enhance the identification of thin ice areas. The detection of the thin ice areas is first based on the AMSR2 data as it has much better spatial resolution (10 km) than the SMOS chart (12.5 km pixel size, but the true resolution is 30-40 km). Some uncertain cases of the AMSR2 based thin ice detection can be resolved with the help of the SMOS thickness chart as SMOS L-band radiometer data is more robust in thin vs. thick ice separation than the higher frequency AMSR2 data. It is envisaged that the SMOS ice thickness chart is incorporated in the FMI ITC production either in later part of winter 2014-2015, or at latest for winter 2015-2016.

In 2015-2016 the dual-polarized SENTINEL-1 EW mode SAR images are used in the ITC production. In addition, RADARSAT-2 ScanSAR images available through MyOcean-2 may be also utilized.

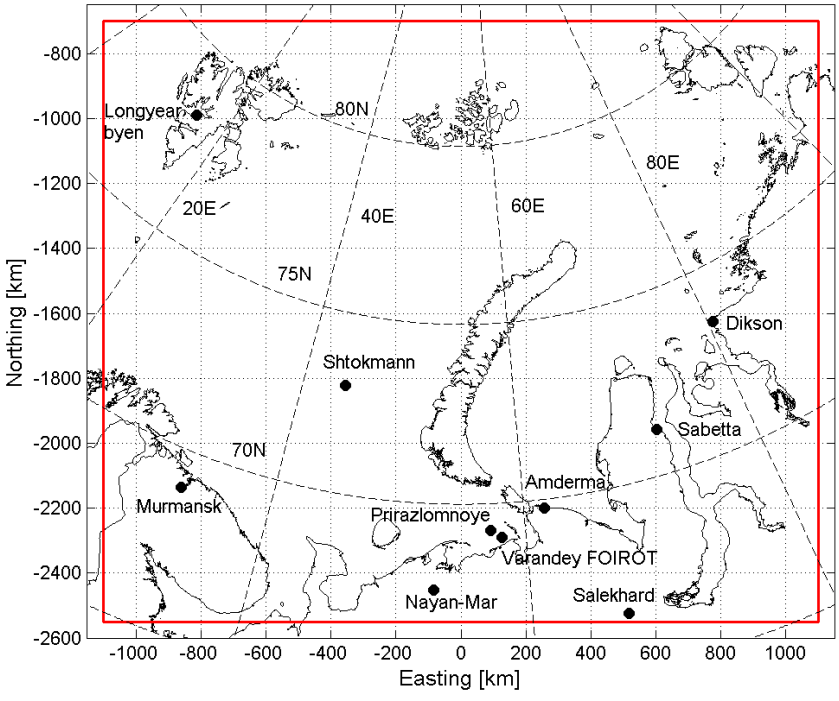

Figure 8. Target area for the FMI multi-sensor data and TOPAZ model based sea ice thickness chart.

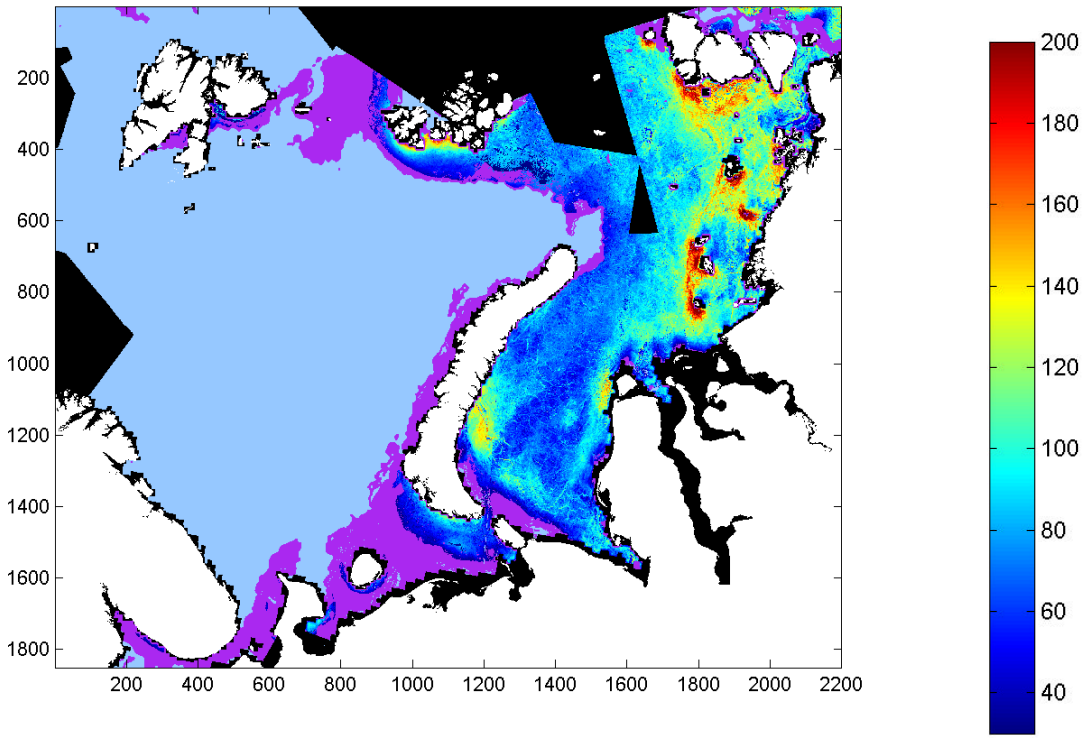

Figure 9. Sea ice thickness chart over the Barents and Kara Seas on 13 Feb 2014. The thickness chart is based on RADARSAT-2 ScanSAR images, AMSR2 radiometer data, and TOPAZ modelled sea ice thickness. Thin ice with maximum thickness of 30 cm is shown with purple colour. Light blue show areas with ice concentration less than 70%.

4.3.2 Algorithm description

The FMI ice thickness chart is based on multi-sensor satellite data: AMSR2 radiometer data (now), SMOS thin ice thickness chart (included later), and RADARSAT-2 ScanSAR HH/HV-polarization images (now); SENTINEL-1 EW mode HH/HV-polarization images replace RS-2 images in 2015, and modelled ice thickness field from the MyOcean TOPAZ-4 coupled ocean-sea ice data assimilation system. Air temperature data from HIRLAM NWP model run by MetNo is used to adjust some thresholds in the thickness chart algorithm.

TOPAZ-4 run by Metno is the latest version of TOPAZ, a coupled ocean-sea ice data assimilation system for the North Atlantic Ocean and Arctic with a horizontal resolution of about 12-16 km (Sakov et al. 2012, Bertino and Lisæter 2008). It provides real-time operational products of the state of the ocean and sea-ice. The model system consists of an ocean model and a dynamic-thermodynamic sea-ice model. TOPAZ-4 represents the main workhorse of the Arctic Marine Forecasting Center (MFC) of the MyOcean project (www.myocean.eu.org) both for short-term forecasting and reanalysis purposes.

The coverage of the FMI ITC over the Barents and Kara Seas is shown in Figure 8. The size of the area is 1850 by 2200 km. The thickness chart is in polar stereographic (PS) coordinate system with reference longitude of 55E. The same reference longitude is used in the AARI ice charts. The

coverage of the ice thickness information near the coast is mainly determined by the TOPAZ-4 model land mask which excludes shallow coastal areas.

4.3.2.1 Overview of the ice thickness algorithm

The ITC production chain has the following main steps.

1. Pre-processing of satellite data, TOPAZ sea ice thickness data and HIRLAM data.
   - Calculation of daily SAR image mosaics at HH- and HV-polarization with 500 m pixel size over the area shown in Figure 8.
   - Calculation of daily sea ice concentration (SIC) chart with 10 km grid size from AMSR2 L2 swath SIC data available from JAXA.
   - Processing of AMSR2 L1R swath 36.5 and 89 GHz brightness temperature data. Final products interpolated to the FMI PS with 1 km pixel size.
   - Interpolation of the daily TOPAZ ice thickness field in PS with -45E reference longitude and grid size of 12.5 km to the 1 km FMI PS grid.
   - Interpolation of the HIRLAM air temperature data to the 1 km FMI PS grid.
2. Identify sea ice areas with SIC>70%. Following steps 3 and 4 are only run over these areas.
3. Thin ice detection. Maximum thickness of detected thin ice is 30 cm.
   - Thin ice detection with the AMSR2 data (thickness of thin ice is not estimated).
   - Over areas not detected as thin ice with AMSR2: assign 1 km pixels with Topaz thickness less than 30 cm to thin ice class.
   - Note: Identification of thin ice areas with the AMSR 2 data (empirical method) is more reliable than using the Topaz, or any other, model data.
4. SAR and TOPAZ based sea ice thickness estimation in areas not detected as thin ice. TOPAZ ice thickness field is modulated locally using the SAR backscatter statistics in sea ice areas not detected as thin ice.
   - In addition, further detection of open water and brash ice based on HH- and HV-polarization SAR data.
5. Combine 3 and 4 for an ice thickness chart with 1 km pixel size. Three SIC classes (<10%, 10-40%, 40-70%) shown when SIC<70%.

4.3.2.2 Input datasets

The needed input datasets are:

- RADARSAT-2 ScanSAR (SCWA mode) HH/HV-polarized SGF path images. Available in NRT through MyOcean.
- SENTINEL-1 Extra Wide Swath (EW) HH/HV-polarized GRD images; replace RS-2 in 2015.
- AMSR2 L1R brightness temperature data; 36.5 GHz data at its original resolution and 89 GHz data sampled to 36.5 GHz resolution. Data is freely available in NRT from JAXA.
- AMSR2 L2 (swath data) sea ice concentration data. Data is freely available in NRT from JAXA.
- SMOS thin ice thickness chart. POLAR ICE product by Univ. Bremen.

- TOPAZ-4 modelled sea ice thickness field. Available through MyOcean.
- HIRLAM 2 m air temperature data. Available from MetNo.

4.3.2.3 Details of the ice thickness algorithm

In the following the steps 1, 3 and 4 are described in more detail.

1. Pre-processing of satellite data

Daily SAR image mosaic

A daily SAR image mosaic with 500 m pixel size is produced by updating the mosaic from previous day with new SAR images acquired during the day. First, the individual calibrated HH- and HV-polarization SAR images are rectified to the FMI PS system with 100 m pixel size. Next, the incidence angle variation of backscatter in the HH-polarization image is compensated by scaling the pixel-wise backscatter coefficient (σ°) values to the incidence angle of 30° using a method developed by Mäkynen et al. (2002) and an empirical incidence angle vs. σ° dependence of -0.24 dB/1°. For the HV-polarization images noise subtraction is conducted, but not the incidence compensation as we have not yet defined it for the HV-polarisation σ°. Finally, 100 m images are processed to 500 m pixel size and added to the daily mosaic. In addition, also mosaics of the incidence angle and SAR acquisition time for each 500 m pixel are produced. A land mask is applied to the mosaics. An example of the SAR mosaics at HH-polarization is shown in Figure 10.

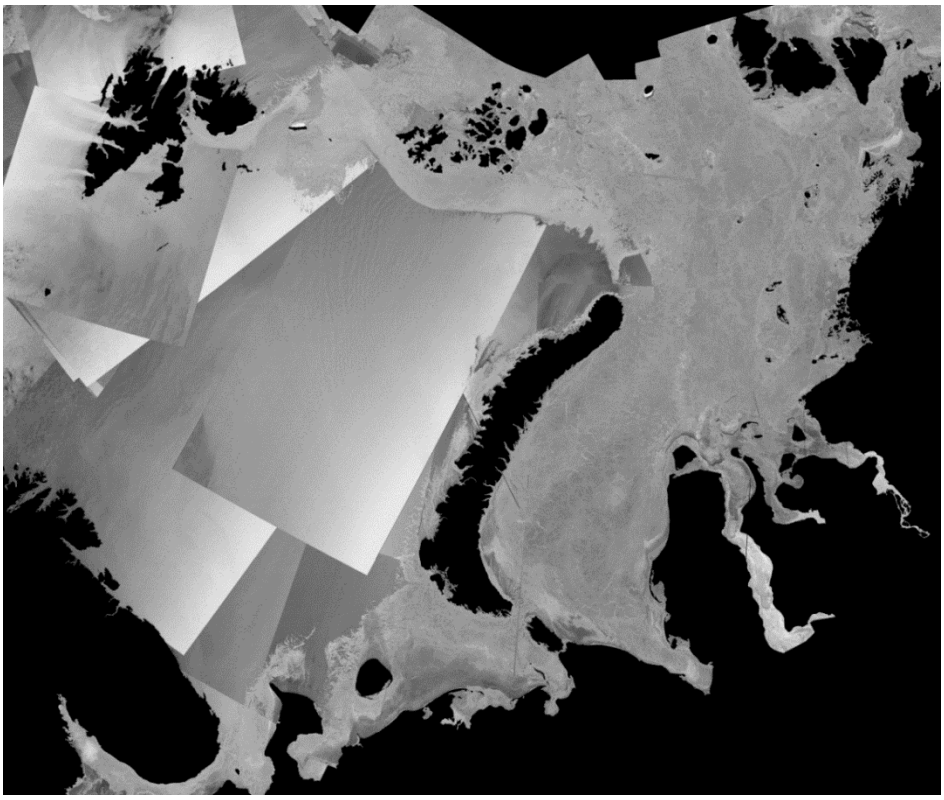

Figure 10. Daily RADARSAT-2 SAR image mosaic at HH-polarization on 13 Feb 2014. Pixel size is 500 m.

Daily SIC chart from the AMSR2 L2 SIC data

Individual AMSR2 L2 SIC swaths are rectified to a 10 km grid over the ITC area. For each grid point a daily average SIC calculated. JAXA produces a daily gridded SIC chart over the Arctic, but it is not available in NRT.

Processing of AMSR2 brightness temperature data

AMSR2 L1R brightness temperatures at 36.5 and 89 GHz from each half-orbit swath covering the ITC area are rectified to the 10 km FMI PS grid. The 10 km pixel size is close to the 36.5 GHz true resolution (antenna footprint) of 7 by 12 km. For each grid point daily average T_B's are calculated. These 10 km average T_B grids are further interpolared to 1 km grid size to match the pixel size of the SAR data analysis. From the T_B data polarization ratio (PR) at 36.5 GHz and gradient ratio (GR) between H-polarized 89 and 36.5 GHz T_B's are calculated:

$$PR36 = \frac{T_{B36V} - T_{B36H}}{T_{B36V} + T_{B36H}} \qquad (1)$$

$$GR8936H = \frac{T_{B89H} - T_{B36H}}{T_{B89H} + T_{B36H}} \qquad (2)$$

These ratios are used in a thin ice detection algorithm. The interpolation of the T_B from 10 to 1 km pixel size requires further investigations as it leads to some artefacts, e.g. T_B smoothing at a sharp thick ice vs. thin ice/open water boundary.

An example of $GR8936H$ at 10 km pixel size is shown in Figure 11. The figure also shows our AMSR2 land mask processed from the NSIDC's AMSR-E 6.25 km Arctic land mask.

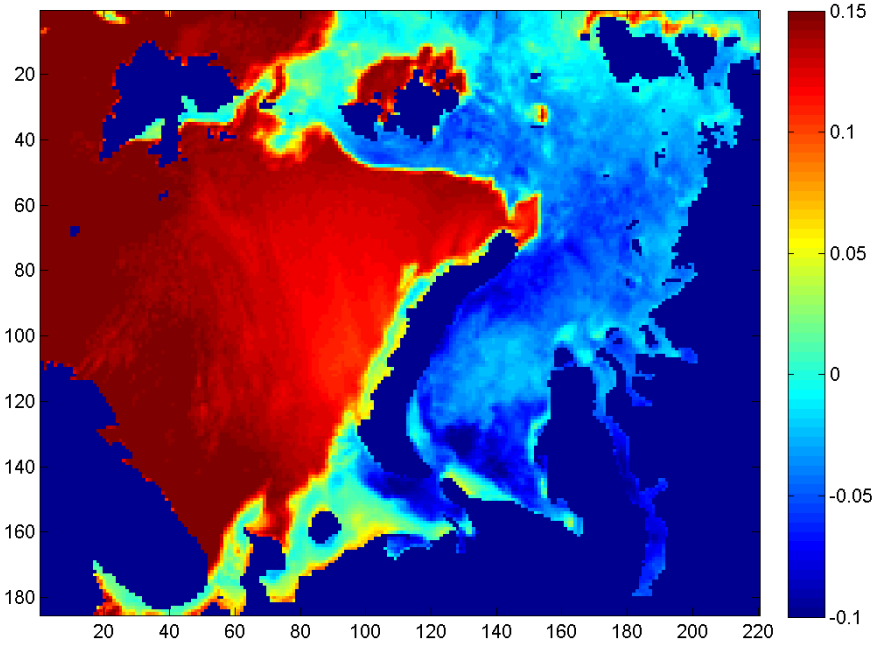

Figure 11. AMSR2 gradient ratio between H-polarized 89 and 36.5 GHz T_B on 13 Feb 2014. A land mask has been applied to the data. Pixel size is 10 km.

3. Thin ice detection using the AMSR2 data

Thin ice detection using the SSMIS and AMSR-E radiometer data was studied previously using data acquired over the Barents and Kara Seas during three winters (Nov-Apr) in 2008-2011 (Mäkynen and Similä 2014). Reference data for the thin ice detection were thin ice thickness charts calculated using MODIS based ice surface temperature and HIRLAM NWP data (Mäkynen et al. 2013). Based on the large dataset we showed that the radiometer data has a large potential in the thin ice identification problem, if the focus in the retrieval is to retrieve thin ice class instead of an attempt to estimate the mean ice thickness of the underlying thin ice field. In the dataset the estimation of thin ice thickness was not possible with significant accuracy due to the large scatter between MODIS ice thickness and the radiometer data. This is opposite to many previous studies, e.g. Tamura and Ohshima (2011), and could be a study region related (here Barents and Kara Seas), but more likely it is due to a much larger dataset than in any previous study, including besides thin ice in polynyas also thin ice in the marginal ice zone and thin ice areas from freeze-up period.

Both the detection of thin ice here and thin ice thickness estimation in previous studies using radiometer data is based on the difference of thin ice vs. thick ice emission properties. The thin ice emission properties depend significantly on near surface salinity which on the average decreases with increasing ice thickness (Naoki et al. 2008). Thus, T_B increases and PR and GR decrease with the increasing thin ice thickness.

Detailed relationships were studied between MODIS ice thickness and different AMSR-E and SMISS PR or GR ratios calculated from the 36/37 and 89/91 GHz T_B data, and and set up thresholds for the thin ice detection and maximum thicknesses of the detected thin ice. We also studied if the PR or GR signatures, and thus, the thresholds and maximum ice thicknesses, depend on the daily mean T_a which was used as a proxy for the daily mean T_s, and further, for thin ice surface condition. The details of our study can be found in Mäkynen and Similä (2014).

The results for different one-dimensional PR and GR parameters in the thin ice detection led to the conclusion that the AMSR-E $PR36$ and $GR8936H$ would be the best parameters when a two-dimensional classifier is constructed. These two parameters behave somewhat differently for thin and thick ice classes. We adopted the linear discrimination analysis (LDA) as our statistical tool. Here the resulting LDA score is calculated as:

$$LDA_{SC} = b_1 \cdot GR8936H + b_2 \cdot PR36 + b_3, \qquad (3)$$

i.e. it is a weighted sum of the two signatures in question. The coefficient vector $b = [b_1, b_2, b_3]$ was statistically determined and its values are $[100, 50, -0.8]$. The thin vs. thick ice separation is based on the LDA score thresholding. The classification accuracy is described with two types of errors: type I error - misclassification of thicker ice as thin ice, and type II error - misclassification thin ice as thick ice, i.e. thin ice is not detected.

Using this approach thin ice areas with maximum thickness of 30 cm could be separated from thicker ice fields with both type I and II errors being 19%, if the statistically optimal LDA parameters and threshold are applied. The error rates were determined using the MODIS ice thickness charts. The two error rates can be easily adjusted by changing the LDA score threshold, see Table 3. Thin ice detection with the AMSR-E $PR36$ and $GR8936H$ using linear discrimination analysis. Grid size of the data is 12.5 km. Results with 1-D $GR8936H$-thresholding shown for comparison.. When the

threshold increases then the type I error decreases and the type II error increases, and thus, it is not possible to detect both thin and thick ice areas with high accuracy.

Type I and II errors are likely mainly caused by variation of thin ice surface properties, e.g. surface roughness (pancake ice, floe size, rafting etc.), surface state (dry, wet, brine skimmed etc.), and occurrence of a dry snow layer or frost flowers on ice.

Table 3. Thin ice detection with the AMSR-E $PR36$ and $GR8936H$ using linear discrimination analysis. Grid size of the data is 12.5 km. Results with 1-D $GR8936H$-thresholding shown for comparison.

Parameter	Samples	Threshold	h_{it} [cm]	Type I Error $h_i > h_{it}$ as thin ice [%]	Type II Error undetected thin ice [%]	h_i>30 cm as thin ice [%]
$GR8936H$	25295	0.0	25	16	27	11
$GR8936H$ and $PR36$	12647	0	25	21	21	11
$GR8936H$ and $PR36$	12647	0	30	19	19	19
$GR8936H$ and $PR36$	12647	0.5	30	11	27	11
$GR8936H$ and $PR36$	12467	1.0	30	4	37	4

For the ITC construction it is of major importance that thick sea ice is not classified as thin ice. Thus, we have currently set the LDA score threshold to a high value of 1.9 when the daily mean air temperature (T_{am}) is below -10 °C. In higher temperatures the threshold is somewhat modified. This high threshold gives very small type I error, but a large fraction of thin ice remains undetected (high type II error). The threshold is a tuning parameter in our LDA classification and its optimal value will be further studied using the winter 2014-2015 AMSR2 data.

In general, the constructed classifier worked rather robustly as indicated by the relative small error rate variation between the three analysed winters (Mäkynen and Similä 2014).

We are using currently the LDA parameters determined with the AMSR-E data also for the AMSR2 data. Our plan to is determine if any modifications are needed using combined AMSR2 data and MODIS ice thickness charts for the winter 2014-2015.

Filtering, or correction, of $PR36$ and $GR8936H$ pixels contaminated with atmospheric effects is currently omitted. Our preliminary analysis suggested that this does not lead to a large increase of the type I error (misdetection of thick ice as thin ice). However, this issue requires further studies.

We likely will change to use individual L1R swath based ratios in the thin ice detection instead of the daily average ratios, as in the swath data the atmospheric effects on the T_B can be estimated better and badly contaminated T_B pixels filtered out more reliably. In this case each pixel has several cases of thin vs. thick ice detections (same as number of daily swaths over a pixel) which allows some statistical rules/thresholds for the overall thin ice detection in a pixel.

Future studies also includes to investigate if it is possible to divide the current thin ice class, max thickness 30 cm, to at least two classes, e.g. 1 to 15 cm (nilas and gray ice) and 15- 30 cm (gray-white ice),using the combination of the AMSR2 LDA score and TOPAZ modelled thickness.

An example of the AMSR2 based thin ice detection is shown in Figure 12.

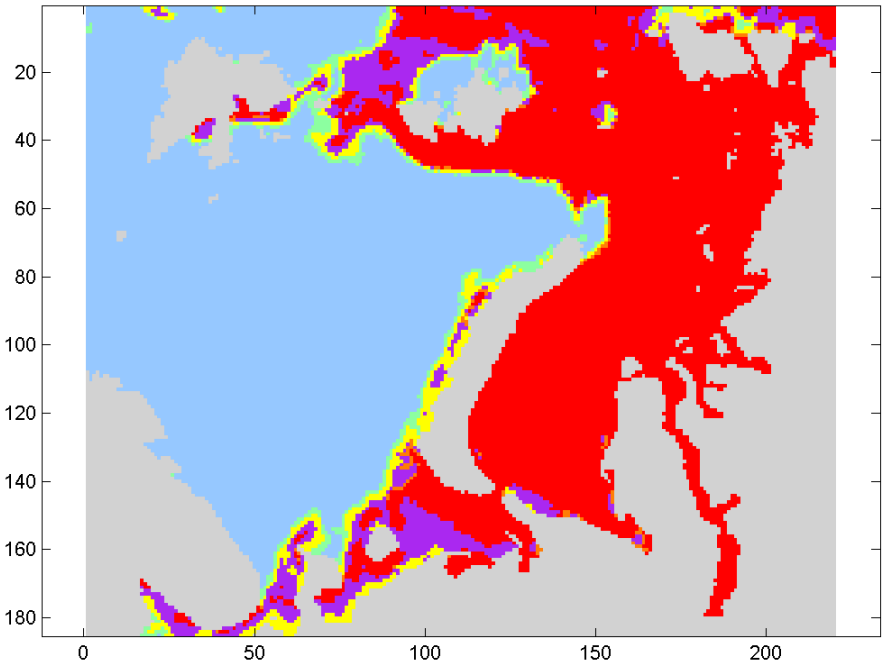

Figure 12. Thin ice detection with the AMSR2 *PR*36 and *GR*8936*H* using linear discrimination analysis on 13 Feb 2014. Red shows areas with SIC>90%, orange is 70-90%, yellow is 40-70%, green is 10-40%, light blue is <10%, and purple is detected thin ice (max thickness 30 cm). SIC in detected thin ice areas is over 70%. Pixel size is 10 km.

4. SAR and TOPAZ based sea ice thickness estimation

Sea ice backscattering at C-band co-polarizations under dry snow conditions is dominated by the ice surface scattering, e.g. (Carlström and Ulander 1995; Dierking et al. 1999). Thus, the σ° magnitude depends mainly on the small (mm-scale) and large (cm to m scale) surface roughness. This suggests a statistical connection between sea ice deformation and σ°: when sea ice deformation increases then also σ° increases. This has been observed empirically in many studies, e.g. for the Baltic Sea ice in (Mäkynen and Hallikainen 2004).

We have studied earlier in detail a link between sea ice C-band HH-polarization σ° signatures from ENVISAT IMP/APP SAR images and ice freeboard (i.e. height variation) statistics based on airborne 3-D laser scanner data (Similä et al. 2010). The datasets were collected during a CryoSat calibration-validation campaign (CryoVex 2005) in March 2005 in the Baltic Sea. In addition, Sea ice thickness was measured with helicopter-borne EM sensor. The analysis between ice deformation and σ° statistics was conducted in resolution of 300 m. The variance of the mean freeboard increased with increasing mean freeboard with the chosen window size (300 m) up to the mean freeboard of 15 cm. This multiplicative character of sea ice cover formed the basis by which we expected that the σ° response, which depends mainly on the ice surface roughness, provides information on the sea ice thickness. A nonlinear regression model with three control variables, σ°, the dominant thickness of the level ice which has deformed, and a variable accounting the effect of the SAR incidence angle, was established to predict the variation of the ice freeboard, and also, sea ice thickness.

One important observation by Similä et al. (2010) that is utilized here is the linear dependence between σ° and fraction of level ice at all SAR incidence angles, see Figure 13. In order to utilize this result here we first converted the ENVISAT σ° values to corresponding RADARSAT-2 σ° values (these sensors have different resolutions, noise levels etc.). We assume that in a σ° interval of [-20, -11] dB the linear relationship between ice deformation and HH-polarization σ° holds for the RADARSAT-2 data acquired over the Barents and Kara Seas and processed to a daily mosaic with 500 m pixel size. The σ° values outside this interval are treated differently. Sea ice thickness in the TOPAZ model refers to equivalent ice thickness, i.e. thickness which corresponds to the uniform distribution of ice mass inside a grid cell. Deformed ice is also included in the TOPAZ modelled thickness. We make an assumption that the fraction of level ice in a single TOPAZ cell is on the average 60%. This assumption is then used as a starting point to modify the TOPAZ thickness:

- The CryoVex 2005 results indicate that a HH-polarization σ° threshold value of -15.5 dB corresponds approximately to the assumed deformation (60%) inside a TOPAZ grid cell.
- If σ° equals to the threshold then the TOPAZ thickness is kept as it is. If σ° is smaller (larger) than the threshold the TOPAZ thickness is decreased (increased). Here σ° must be within the interval of [-20, -11] dB.

Thus, spatial variation of ice thickness at finer scale (here 1 km) than in the TOPAZ model grid (12.5 km) is introduced through the spatial variation of σ°. In quantifying the increase/decrease rate (i.e. scaling factor) of the TOPAZ thickness according to σ° the CryoVex 2005 results were utilized. Maximum factor to increase the TOPAZ thickness is 1.4. It is noted that the σ° threshold (current value -15.5 dB) is a tuning parameter. Its value was selected so that the ice masses produced by the TOPAZ and the thickness chart were close to each other.

Finally, σ° outside of interval [-20,-11] dB, and the first principal component score from the combination of the HH- and HV-polarization SAR images are used identify to brash ice areas and additional open water areas (and very thin ice) missed with the AMSR2 data. Brash ice (includes also pancake ice) occurs mainly in the ice edge zone and has typically very high backscatter, although its thickness can be very variable. For brash ice only coarse thickness estimation is currently possible.

It is noted that all above σ° thresholds are for the incidence angle scaled RS-2 HH-polarization images (incidence angle scaled to 30°). For using the SENTINEL-1 EW SAR images in the ITC production we must first convert the σ° based classification rules for RADARSAT-2 to SENTINEL-1, because these two sensors have different noise floors, resolutions, and effects of speckle.

Our plan is to utilize better HV-polarization images, currently there are only used in PCA analysis together with the HH-polarization images to identify brash ice areas. As the HV-polarization σ° is more sensitive to degree of ice deformation (e.g. Mäkynen and Hallikainen 2004), its use, together with the HH σ°, should enhance SAR and TOPAZ based the ice thickness estimation. However, the usage of the HV-polarization images is typically limited by the high SAR noise floor compared to the sea ice σ° signatures. At low signal-to-noise ratios the noise subtraction from the measured σ° values may not work properly. The noise floor of the SENTINEL-1 is expected to be higher than that of the RADARSAT-2, -22 dB vs. -28.5 dB noise equivalent σ°, respectively.

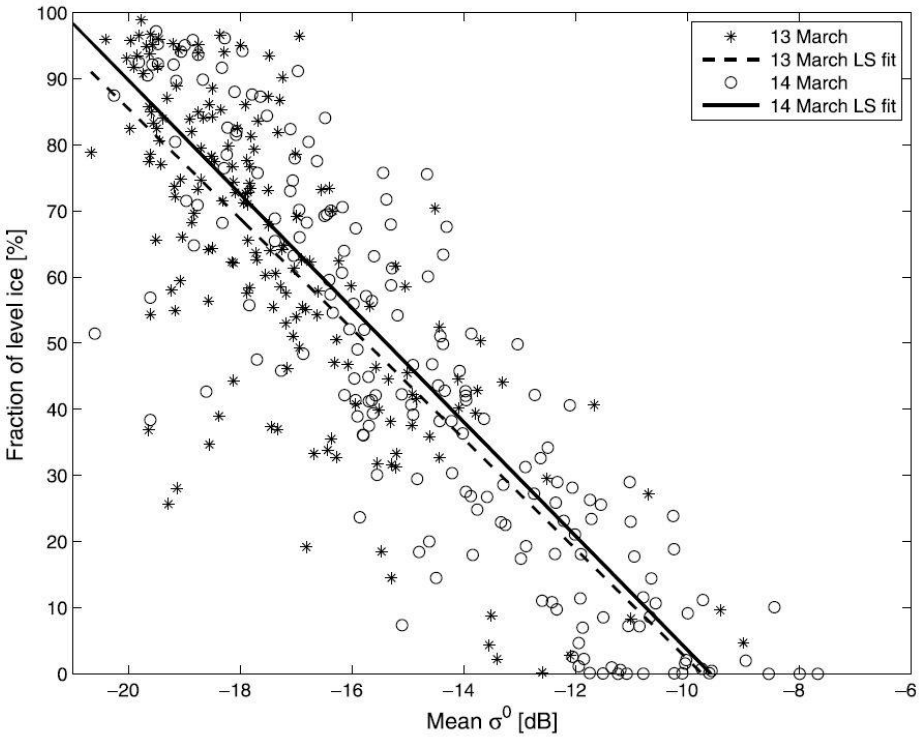

Figure 13. Mean C-band σ° at HH polarization versus fraction of level ice within 300 x 300 m windows (Similä et al. 2010). Data were collected in the CryoVex 2005 campaign in the Baltic Sea. Fraction of level ice was estimated from airborne laser scanner (ALS) data. The mean σ° values are from ENVISAT IMP/APP images.

4.3.3 Output formats

The FMI ice thickness chart is distributed in the following two formats which both are suitable for off-shore end-users with low bandwidth internet connections:

- GeoTIFF image: contains sea ice thickness, geolocation, and date information. This format is targeted for POLAR ICE visualization software.
- Map image (e.g. png-file) of the thickness chart (see example in Figure 9): can be viewed with any image viewing software, contains only very coarse geolocation information.

4.3.3.1 GeoTIFF-image

Following information is given in the filename and header of the GeoTIFF image:

- Geolocation information: corner coordinates in the polar stereographic coordinate system, pixel size (1000 m), details of the coordinate system (datum, reference longitude).
- Product name, and product provider.
- Version of the processing algorithm.
- Product generation date and time in UTC.

The sea ice thickness data and various masks have the following 8-bit coding:

pixel value 0 = open water

pixel value 2 = no data area over ocean

pixel value 5 = combined mask of input datasets and land area

pixel value 10 = land mask

pixel value 15 = reserved for thin ice type 1, thickness e.g. 1-15 cm

pixel value 20 = thin ice class (1-30 cm), or thin ice type 2, thickness e.g. 16-30 cm

pixel values from 31 to 255 = sea ice thickness in [cm]

4.3.4 Validation

We don't have yet any in-situ or airborne EM-sensor ice thickness data for the validation of the FMI ice thickness chart (ITC). In the ESA ANISTIAMO project ITCs for Jan-Apr 2014 were compared to the AARI weekly ice charts for the Barents and Kara Seas. The AARI chart is available in digital SIGRID-3 format. It is made by professional ice analysts who have a long experience on ice conditions in the Kara and Barents Seas. They use the remote sensing data (from Russian and other satellites) and in situ-measurements from the Russian icebreakers. They also inspect sea ice model results. Still the end result is rather subjective (as for all manual ice charts), and the accuracy of the chart is currently unknown, or at least unpublished.

The ice thickness information in the AARI chart has much coarser spatial resolution than that of ITC. Hence, the wider ITC thickness distributions corresponding to an AARI ice type class are natural. For all AARI ice type classes the median thickness in ITC was within the AARI mean ± std thickness interval, see Figure 14. The growth of the mean thickness is very similar in both charts up to 0.8 m. In the thicker ice classes the AARI ice estimates are somewhat higher but in all cases the 60 % ITC thickness interval covers the whole AARI mean ± std interval and is actually significantly larger. This can be partly explained by the finer resolution in ITC. No drastic differences between the two charts were observed. Typically the absolute differences were less than 20 cm. The largest discrepancies between the two charts occurred especially in the coastal areas of the Kara Sea and around the small islands in the northwest Kara Sea.

One of the requirements for a thickness chart is that it conserves the ice mass. As several different data sources are used to construct our ITC, this property is not trivially satisfied. This feature is illustrated in Figure 15 by the temporal change of the mean ice thickness in the Kara Sea according to the ITC, AARI chart and the TOPAZ model. The size of the area used in the calculations varied according to the available SAR coverage. This causes some fluctuation observed in Figure 15. Sometimes the reason for the fluctuation is purely geophysical, i.e. the ice conditions changed drastically in the area; e.g. in the AARI chart number 11 the mean thickness decreases because of opening of an exceptionally large polynya near the Ob Bay. On average the mean thickness according to the TOPAZ model and ITC chart are of the same magnitude. This accords with our objective because the main role of the SAR data is to refine the spatial distribution of ice mass provided by the coarse resolution TOPAZ model. Compared to the AARI chart mean thickness the mean thickness in the ITC charts is larger early in the winter and slightly lower in April.

In POLAR ICE further validation activities will be conducted with all available data, e.g. with data from Norwegian Young sea ICE cruise (N-ICE2015).

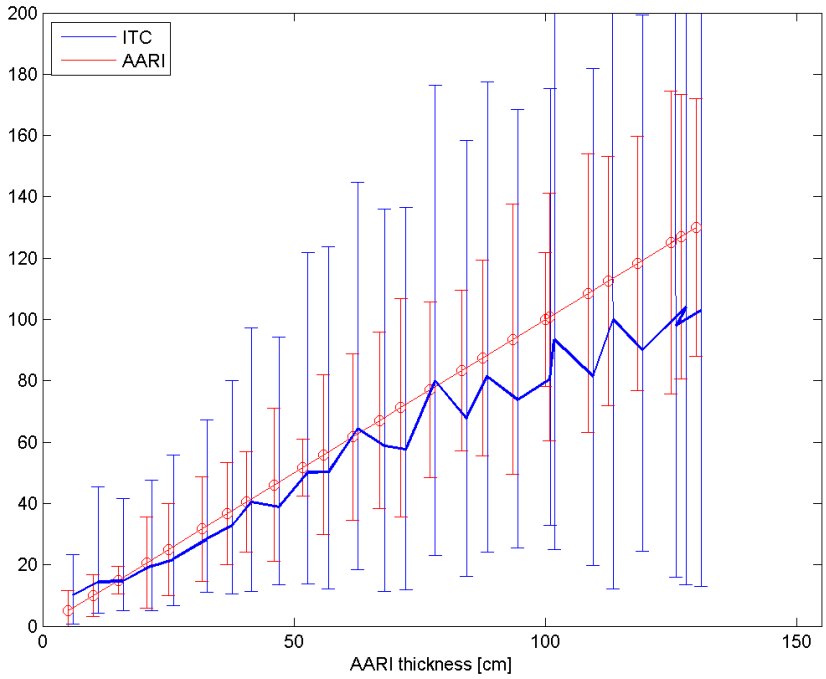

Figure 14. Comparison between ice thickness data in the AARI ice charts and FMI ice thickness chart (ITC). The AARI chart segment-wise mean ice thickness and standard deviations are marked by red. The thickness distribution in ITC corresponding different AARI ice thickness classes are marked by blue. They are calculated for the same polygons as the AARI ice thickness. The lower blue bar represents the 20% quantile and the upper blue part 80% quantile of the ITC thickness distribution for a specific AARI thickness class.

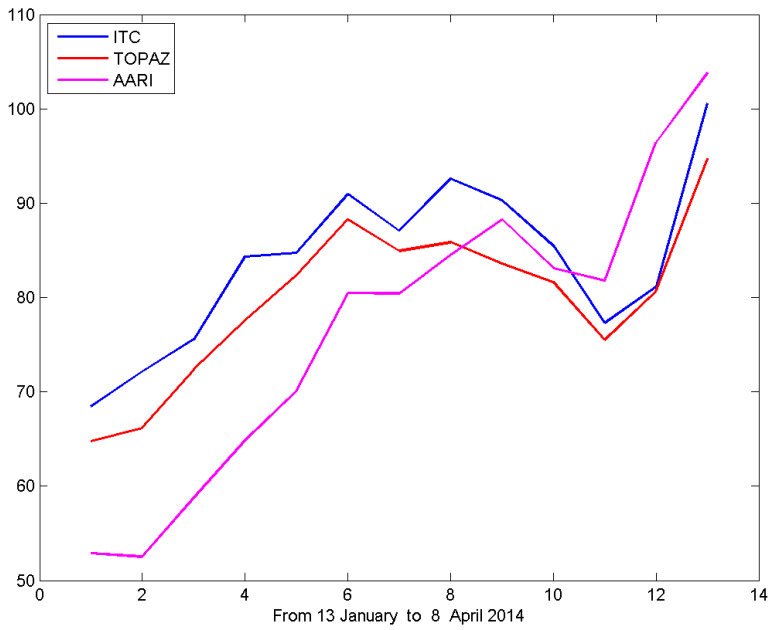

Figure 15. The average thickness per pixel (1 km resolution) within time interval of one week covering the tim eperiod from 13 January to 8 April 2014 in the Kara Sea.

4.3.5 Product summary

Table 4. General properties of the FMI sea-ice thickness chart for the Barents and Kara Seas.

Product description	Sea ice thickness based on multisensor satellite data and MyOcean TOPAZ model. Thin ice (max thickness 30 cm) identified AMSR2 radiometer and TOPAZ model data. For thicker ice areas SAR data are used to modulate locally the TOPAZ ice thickness field.
Satellite input data	AMSR2 radiometer data, RADARSAT-2 ScanSAR or Sentinel-1 EW mode images, SMOS thin ice thickness chart.
Model input data	MyOcean TOPAZ-4 ice thickness data, HIRLAM 2 m air temperature data.
Sea ice parameter(s)	First-year ice thickness up to 2.5 m when sea ice concentration (SIC) is larger than 70%. For SIC less than 70% three SIC classes are shown. Thin ice with maximum thickness of 30 cm as one class.
Coverage	Barents and Kara Seas
Update interval	Every 1-3 days in winter conditions (Oct/Nov to May) depending on the SAR coverage.
Spatial resolution	1 km
Delivery time	< 12 h - thickness chart is based on daily gridded data On morning (before 9 UTC) a thickness chart is produced for previous day.
Formats	GeoTIFF-image, map image (png-file).
Chart size	3.88 MB without compression, ~800 kB with compression

4.3.6 References

Bertino, L., and K. A. Lisæter, "The TOPAZ monitoring and prediction system for the Atlantic and Arctic Oceans," *Journal of Operational Oceanography*, 2008, 15–18, 2008.

Carlström, A., and L. M. H. Ulander, "Validation of backscatter models for level and deformed ice sea ice in ERS-1 SAR images," *Int. J. Remote Sens.*, 16(7), 3245-3266, 1995.

Dierking, W., A. Carlström, and L. H. M. Ulander, "The Effect of inhomogeneous roughness on radar backscattering from slightly deformed sea ice," *IEEE Trans. Geosci. Remote Sensing*, 35(1), 147-159, 1997.

Mäkynen, M., T. Manninen, M. Similä, J. Karvonen, and M. Hallikainen, "Incidence angle dependence of the statistical properties of the C-band HH-polarization back-scattering signatures of the Baltic Sea ice," *IEEE Trans. Geosci. Remote Sensing*, 40(12), 2593-2605, 2002.

Mäkynen, M., and M. Hallikainen, "Investigation of C- and X-band backscattering signatures of the Baltic Sea ice," *Int. J. Remote Sens.*, 25(11), 2061-2086, 2004.

Mäkynen, M., B. Cheng, and M. Similä, "On the accuracy of the thin ice thickness retrieval using MODIS thermal imagery over the Arctic first year ice," *Annals of Glaciology*, 54(62), 87-96, 2013.

Mäkynen, M., and M. Similä, “Thin ice detection in the Barents and Kara Seas with AMSR-E and SSMIS radiometer data,” submitted to *IEEE Trans. Geosci. Remote Sensing*, Aug 2014.

Naoki, K., J. Ukita, F. Nishio, M. Nakayama, J. C. Comiso, and A. Gasiewski, “Thin sea ice thickness as inferred from passive microwave and in situ observations,“ *J. Geophys. Res.*, 113, C02S16, 2008.

Sakov, P., F. Counillon, L. Bertino, K. A. Lisæter, P. R. Oke, and A. Korablev, “TOPAZ4: an ocean-sea ice data assimilation system for the North Atlantic and Arctic,” *Ocean Sci.*, 8, 633–656, 2012.

Similä, M., M. Mäkynen and I. Heiler, “Comparison between C band synthetic aperture radar and 3-D laser scanner statistics for the Baltic Sea ice,” J. *Geophys. Res.*, 115, C10056, doi:10.1029/2009JC005970, 2010.

Similä, M., M. Mäkynen, B. Cheng, and E. Rinne, “Multisensor data and thermodynamic sea-ice model based sea-ice thickness chart with application to the Kara Sea, Arctic Russia,” *Annals of Glaciology*, 54(62), 241-252, 2013.

Tamura, T., and K. I. Ohshima, “Mapping of sea ice production in the Arctic coastal polynyas,” *J. Geophys. Res.*, 116, C07030, 2011.

4.4 NR Sea ice thickness product

4.4.1 Overview

Norsk Regnesentral's (NR) ice thickness product for thin ice relies on the temperature difference between the ice/snow surface and the water below the ice. For thin ice, the relatively warm water will significantly contribute to heating of the ice surface. However, as the ice grows thicker (or accumulates a layer of snow on top) this heating effect grows weaker, and the surface temperature will be more dependent on the atmospheric conditions. For thin ice it is therefore possible to estimate the ice thickness, by modelling the heat balance on the ice surface using satellite based ice surface data and numerical weather forcing data.

This algorithm makes use of the thermal bands of the VIIRS sensor on the Suomi-NPP satellite to estimate the ice surface temperature. This allows estimating the sea ice thickness with the relatively high spatial resolution of 750 m. At this resolution ice-leads and other local structures are visible in the sea ice.

However, using thermal satellite data makes it necessary to reliably detect clouds over sea ice. Due to the difficulty of cloud detection in the Arctic (especially during night) the cloud mask often covers most of the thermal satellite image.

The algorithm assumes cold weather conditions, and is best suited for the freezing period of the ice. Later in the season, temperatures rise, and changes in the structure of the snow surface (e.g. melt ponds) make the thickness estimation inaccurate.

The current version of the algorithm was initially developed in the ESA/PRODEX funded ThinIce project (Figure 16) (Rudjord et al. 2014).

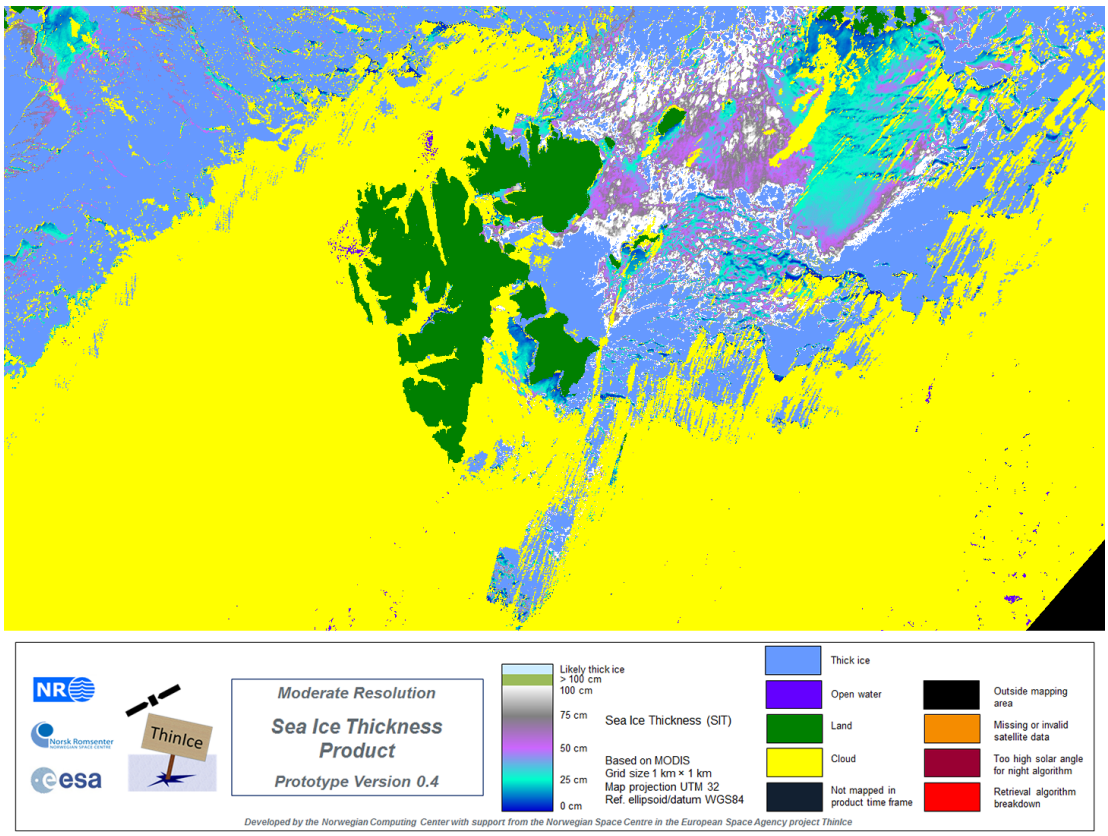

Figure 16. Svalbard, March 7, 2013. Sample thin ice thickness product from the ThinIce project.

4.4.2 Algorithm description

4.4.2.1 Theoretical background

The methodological approach for estimation of the ice thickness from optical thermal data combined with ancillary meteorological data is presented in the following. The ice thickness estimation approach follows Drucker et al. (2003) and Yu and Rothrock (1996) in that it is assumed that the ice is thin, the water temperature is at freezing level and the temperature profile is linear within the ice. The heat flux through the ice is set equal to the atmospheric flux, which allows us to solve for what we call the thermal ice thickness h_T. According to Yu and Rothrock, this linear approximation is valid for ice thicknesses less than about 0.5 m.

According to Yu and Rothrock (1996), the total heat flux on the top surface during the cold season can be decomposed into:

$$F_{total} = F_r - F_l^{up} + F_l^{dn} + F_s + F_e + F_c$$

Where F_r is the solar radiation flux, F_l^{up} is the upwelling longwave flux (the thermal radiation from the ice surface), F_l^{dn} is the down-welling longwave radiation (the thermal radiation from the atmosphere on the surface), F_s is the turbulent sensitive heat flux, F_e is the latent heat flux and F_c is the conductive heat flux (the heat flux from the water to the surface). It is assumed that the surface temperature can be considered constant, giving $F_{total} = 0$.

The longwave fluxes can be described by the Stefan-Boltzmann law for blackbody radiation, giving us $F_l^{up} = \varepsilon_i \sigma T_s^4$ and $F_l^{dn} = \varepsilon_a \sigma T_a^4$ where $\sigma = 5.6704 \cdot 10^{-8} \frac{\mathrm{W}}{\mathrm{m^2 K^4}}$ is the Stefan-Boltzmann constant, $\varepsilon_i = 0.988$ is the emissivity of ice, $\varepsilon_a = 0.7855$ is the effective emissivity of the atmosphere, and T_s and T_a are the temperatures of the ice surface and the atmosphere respectively. T_s can be estimated from the thermal satellite imagery, and T_a is approximated by the air temperature at 2 meters

Following Yu and Rothrock (1996) the turbulent sensible heat flux can be described as

$$F_s = \rho_a c_p C_s u_2 (T_a - T_s)$$

where ρ_q is the air density, c_p is the specific heat of air, C_s is a bulk transfer coefficient, u_2 is the wind speed at 2 meters above the surface.

The latent heat flux is described as in Maykut (1978):

$$F_e = \rho_a L C_e u_2 (f e_{sa} - e_{s0}) \cdot 0.622 / P_a$$

where $L = 2.5 \cdot 10^6$ J/kg is the latent heat of vaporization, C_e is a bulk transfer coefficient, f is relative humidity set to 90%, e_{sa} is the saturation vapour pressure and e_{s0} is the saturation vapour pressure at the surface.

The 2-meter wind speed, u_2, is found from the 10-meter wind speed, u_{10}, by $u_2 = u_{10}/1.27$ based on estimate by Fissel and Tang (1991).

The bulk transfer coefficient C_e for the latent heat flux is found from the 10 meter wind speed using a parameterization by Bentamy et al (2003):

$$C_e = \left(a e^{b(u_{10}+c)} + \frac{d}{u_{10}} + 1 \right) \cdot 0.001$$

Here, $a = -0.146785$, $b = -0.292400$, $c = -2.206648$ and $d = 1.6112292$ are constants. For the bulk transfer coefficient for turbulent sensible heat, we use the relation $C_s = 0.98 \cdot C_e$, as in Wang et al. (2010).

The air density of wet air is estimated using the relation of Wang et al. (2010):

$$\rho_a = \frac{100 P_a}{R_{gas} T_v}$$

Here T_v is the surface air virtual temperature given by $T_v = (1 + 0.608x) T_a$. $P_q = 1013.25$ hPa is the air pressure and the gas constant is $R_{gas} = 287.1$ J/kgK. x is here the specific humidity, which is found as $x = f x_s$, were x_s=0.003767 kg/kg is the specific humidity of saturated air.

The specific heat of air is found from specific humidity by $c_p = 1004.5(1.0 + 0.9433x)$ J/K.

The saturation vapour pressure is described using a parameterisation by Maykut (1982), where it is expressed as a function of temperature. We let $e_{sa} = e_s(T_a)$ and $e_{s0} = e_s(T_s)$.

We follow Yu and Rothrock in that we assume that the conductive heat flux, F_c, can be expressed as:

$$F_c = k_i k_s (T_f - T_S)/(k_S H + k_i h)$$

Here, k_i and k_s are the thermal conductivity of ice and snow, respectively, T_f is the freezing temperature of seawater, modelled as $T_f = -0.055\ S_w$, where the seawater salinity is assumed to be $S_w = 31.0$ parts per thousand (ppt). H is the thickness of the ice and h is the thickness of snow on top of it. The conductivity of snow is set to $k_s = 0.31$, and the conductivity of sea ice is assumed to be $k_i = k_0 + \beta S/(T_i - T_0)$. Here $k_0 = 2.034 \frac{\mathrm{W}}{\mathrm{mK}}$ is the conductivity of pure ice, $\beta = 0.13 \frac{\mathrm{W}}{\mathrm{m^2 kg}}$, $T_0 = 273.15\mathrm{K}$ is the freezing point of pure water and T_i is the temperature within the ice. T_i is assumed to be equal to the surface temperature $T_i = T_s$. S is the sea ice salinity, measured in parts per thousand, and is modelled according to Cox and Weeks (1974) as

$$S = 12.24 - 19.39H \text{ for } H \leq 0.4$$

$$S = 7.88 - 1.59H \text{ for } H > 0.4$$

The estimate for the snow depth on the sea ice is based on the empirical relationship described by Doronin et al (1971):

$$h = 0 \quad \text{for } H \leq 5\mathrm{cm}$$

$$h = 0.05H \quad \text{for } 5\mathrm{cm} \leq H < 20\mathrm{cm}$$

$$h = 0.1H \quad \text{for } H \geq 20\mathrm{cm}$$

However, this relationship is found to be very inaccurate for ice very close to land. In these areas the snow layer is found to be much deeper. This is presumably due to either increased precipitation close to the shoreline, or winds transporting the snow closer to land. In order to compensate for this effect, the model is adjusted by including a "land proximity factor", L, a correction factor dependent on the distance from the shoreline.

$h = 0$	for	$H \leq 5\mathrm{cm}$
$h = 0.05H \times L$	for	$5\mathrm{cm} \leq H < 20\mathrm{cm}$
$h = 0.1H \times L$	for	$H \geq 20\mathrm{cm}$

A map describing the land proximity factor for each grid cell was made by Gaussian smoothing of a land mask with a standard deviation of 5 km. The land proximity mask was then scaled so to have a value of *L=3.5* at the shoreline and *L=1.0* further away. This causes the estimated snow depth to be unchanged far from land, while grid cells a few kilometres from the shoreline will have a higher estimated snow depth.

When considering night scenes, the solar radiation is vanishing, $F_r = 0$. However, when considering daytime images, this heat flux is also modelled. As described in Yu and Rothrock (1996) it can be described with two terms as:

$$F_r = (1 - \alpha_S) F_{SW} - I_0$$

Here F_{SW} is the incoming shortwave radiation, α_S is the surface albedo and I_0 is the radiation flux passing through the ice. The last term can be described as $I_0 = i_0(1-\alpha_S)F_{SW}$ where the transmittance, i_0, is the fraction of the shortwave flux that passes through the ice. This leads to the solar radiation heat flux:

$$F_r = (1-\alpha_S)(1-i_0)F_{SW}$$

For describing the shortwave heat flux, F_{SW}, we use a parameterisation by Shine (1984)

$$F_{SW} = \frac{S_0 \cos^2\theta}{1.2\cos\theta + (1+\cos\theta)\cdot 0.001 e_0 + 0.0455}$$

$S_0 = 1367 Wm^{-2}$ is the solar constant at the atmospheric top, θ is the solar zenith angle. Here $e_0 = f e_{s0}$ is the surface water vapour pressure, where e_{s0} is the saturation vapour pressure in hPa, and f is the relative humidity, assumed to be $f = 90\%$.

The saturation vapour pressure is found using the parameterization by Maykut (1978).

Both the albedo, α_s, and the transmittance, i_0, of bare and snow covered ice are parameterised as functions of ice or snow thickness, as described in Grenfell (1979).

All of the above assumptions and models are combined to describe the different heat fluxes, which are then inserted into the heat balance equation. Unfortunately, due to dependencies of ice thickness in modelling several of the parameters, the resulting equation is not analytically solvable for H. As the ice thickness is not initially known, the equation is solved several times with different initial assumptions.

The interval of interest is considered to be ice thicknesses between 0 and 1.0 meter. This interval is split in several sub-intervals of 0 cm < H < 5 cm, 0 cm < H < 10 cm, and so on. For each of these intervals the entire estimation is performed using an assumed ice thickness equal to the mean value on the interval. This assumed ice thickness value is used to estimate the albedo, transmittance and snow depth used in the ice thickness estimate. In the end each of these assumptions yield different ice thickness estimates. Then the ice thickness estimate which is closest to its initial assumption is selected.

Given values for surface temperature, air temperature and wind speed, this framework can now be used to estimate the ice thickness. The surface temperature, T_s, is found from VIIRS thermal imagery, using Key's algorithm for surface temperature (Key, 1997), but using coefficients for the thermal bands of VIIRS (Key, 2014). The air temperature T_a and the wind speed, u_2, are obtained from HIRLAM data, provided by Norwegian Meteorological Institute (MET). These meteorological data cover most of the arctic, with the exception of the area around the Bering Strait. For future expansion of the product coverage, data from Global Forecast System (GFS) will be used.

After the ice thickness estimation, areas with too thick ice were masked out using a simple threshold, masking estimates of more than 1 m ice thickness.

Finally, the cloud mask provided with the VIIRS data is applied to remove cloud covered areas from the product.

4.4.2.2 Processing chain

The processing chain is coded in IDL, using a Python framework. A high-level conceptual diagram of the proposed Thickness of Thin Ice (TTI) processing chain is given in Figure 17.

The main data elements and modules of the processing chain are:

1. *VIIRS thermal data*: Suomi NPP VIIRS data downloaded from NASA.
2. *GFS data*: 10-m air temperature and 10-m wind speed data, downloaded automatically from NOAA's data server.
3. *VIIRS Cloud Mask*: VIIRS Cloud Mask product provided with the VIIRS data.
4. *Static land mask*: Land mask removing land areas from the product.
5. *Skin Surface Temperature Retrieval*: Estimating the surface temperature of snow and ice.
6. *Project*: Projection of the input data to the output grid (EASE and/or UTM).
7. *Thick Ice Mask Generation*: Masking out regions of thick ice.
8. *Thin Ice Thickness Estimation*: Estimation of ice thickness based on surface temperature and atmosphere data. Applying masks.
9. *Merge scenes*: Products are mosaicked to form one daily product.
10. *Export*: Export the product to GeoTIFF file, as well as a PNG quick look image
11. *Thin Ice Thickness Product*: Map showing the extent and thickness of thin ice in GeoTIFF format.

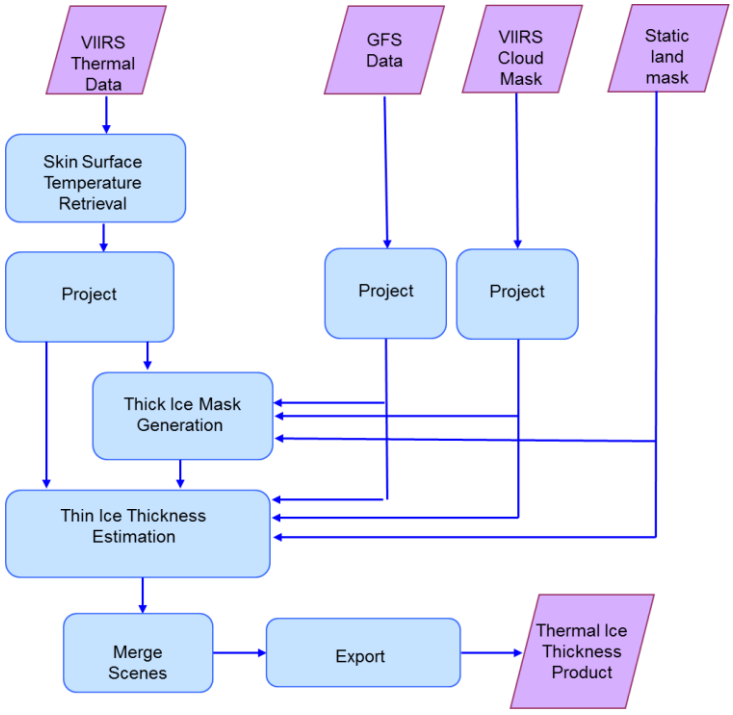

Figure 17. A figure showing the processing chain for the ice thickness product based on thermal imagery.

4.4.3 Output formats

The product consists of two files.

- One GeoTIFF file containing a raster map, showing the sea ice cover, with numerical values of the ice thickness estimate in each pixel where this is available.
- A png quicklook file, containing a colour image for convenient lookup.

4.4.3.1 File name conventions

The product files will be on the format:

<product>_<resolution>_<grid>_<sensor>_<yyyymmdd>_<format>.<extention>

Product: tti (Thickness of Thin Ice)

Resolution: 750m

Grid: The output grid: ease or utm

Sensor: viirs

Yyyymmdd: the year, month and day of the satellite data the product is based on.

Format: geotiff for the GeoTIFF image, pngCol for the png color image.

Extention: .tif for the GeoTIFF image, .png for the png color image.

Thus an example file name is:

tti_750m_ease_viirs_20140325_geotiff.tif

4.4.3.2 Product coding

The GeoTIFF files contain one byte image with geolocation information. The values in each grid cell follows the following convention: values in the range 0-99 represent mask values, while values in the range 100-200 represent ice thicknesses estimates in the range 0 – 100 cm. The product codes are summarized in Table 5.

Table 5. Product codes for thin ice product based on thermal imagery.

0	Not mapped in product time frame
10	Missing or invalid satellite data
20	Clouds
30	Land
40	Water
80	Cell content uncertain
90	Thick ice
101 - 200	Thin ice, estimated thickness: 1 – 100 cm

4.4.4 Validation

A preliminary evaluation of the algorithm under development was performed within the ESA/PRODEX ThinIce project, using data from helicopter-borne electromagnetic sea ice thickness sounding (HEM) [e.g. Renner et al., 2013; Haas et al., 2009]. The HEM system is towed underneath a helicopter at a height of approximately 15 m above the sea ice surface. With a nominal flying speed of 70 knots (36 m s^{-1}), we get measurements every 3 to 4 m with a footprint of about 50 m. The HEM system measures the ice thickness by making use of the difference in conductivity between sea ice and sea water.

The comparison between the HEM and thermal ice thickness datasets yielded a root mean square difference of 41 cm and 56 cm for the 0 to 50 cm and complete range of ice thickness estimates, respectively. The bias for the interval 0 to 50 cm was found to be -28 cm, while the bias was -6 cm when using the complete range of ice thickness estimates. While some of this bias may be due to inaccuracies in the HEM measurements, two kinds of errors were identified in the thermal ice thickness estimates.

When inspecting the ice thickness products manually it was found that they were unstable, and could quickly shift from being accurate to being very inaccurate. This is likely caused by short term changes in the atmospheric conditions which are not accurately described by the atmospheric data (For the ThinIce project, ERA interim was used for atmospheric data). For the ice thickness estimates in Polar Ice, the atmospheric data will be replaced with HIRLAM data provided by MET. Also, during the validation the thick ice mask was not used as it was found to be inaccurate. It is likely that using an improved thick ice mask would significantly reduce the bias by removing inaccurate estimates.

Furthermore the histogram of ice thickness distribution from the products showed a peculiar peak and a sharp drop at 20 cm. This was likely caused by a discontinuity in the snow model, which is planned to be revised.

4.4.5 Product summary

Table 6. Summary of product properties.

Product Description	Sea ice thickness based on thermal satellite imagery
Satellite input data	VIIRS thermal imagery
Model input data	HIRLAM wind and air temperature data. In the future also data from Global Forecast System
Sea Ice parameters	Sea ice thickness up to 100 cm.
Coverage	European Arctic. In the future full Arctic and Antarctic.
Update interval	Daily, but limited by clouds.
Spatial Resolution	750 m
Delivery Time	20 h
Format	GeoTIFF image and PNG map image
Product size	GeoTIFF: ~165MB, PNG-image: ~5.6MB

4.4.6 References

Bentamy, Abderrahim, Kristina B. Katsaros, Alberto M. Mestas-Nuñez, William M. Drennan, Evan B. Forde, Hervé Roquet, 2003: Satellite Estimates of Wind Speed and Latent Heat Flux over the Global Oceans. *J. Climate*, **16**, 637–656.

Cox, G. F. N. and Weeks, W. F, 1974, Salinity variations in sea ice, *Journal of Glaciology,* Vol 13, No 67

Drucker, R., S. Martin and R. Moritz, 2003. Observations of ice thickness and frazil ice in the St. Lawrence Island polynya from satellite imagery, upward looking sonar, and salinity/temperature moorings. *Journal of Geophysical Research,* 108 (C5), 3149.

Fissel,D . B., and C. L. Tang, 1991, Response of sea ice drift to wind forcing on the northeastern Newfoundland shelf, *J . Geophys.Res*., 96, 18, 397-18, 409.

Grenfell, T. C., 1979. The Effects of Ice Thickness on the Exchange of Solar Radiation over the Polar Oceans. *Journal of Glaciology*, 22, 305

Haas, C., J. Lobach, S. Hendricks, L. Rabenstein, and A. Pfaffling (2009): Helicopter-borne measurements of sea ice thickness, using a small and lightweight digital EM system, *Journal of Applied Geophysics*, 67, 234-241, doi:10.1016/j.jappgeo.2008.05.005.

Key, J., J. Collins, C. Fowler, and R. Stone, 1997. High-latitude surface temperature estimates from thermal satellite data. *Remote Sensing Environ*., 61, 302-309.

Key, J., 2014, private communications

Maykut, G. A., 1978. Energy Exchange Over Young Sea Ice in the Central Arctic. *Journal of Geophysical Research,* 83 (C7), 3646.

Maykut, G. A., 1982. Large-Scale Heat Exchange and Ice Production in the Central Arctic. *Journal of Geophysical Research,* 87 (C10), 7971.

Renner, A. H. H., S. Hendricks, S. Gerland, J. Beckers, C. Haas, and T. Krumpen (2013): Large-scale ice thickness distribution of first-year sea ice in spring and summer north of Svalbard, *Annals of Glaciology*, 54(62), 13-18, doi:10.3189/2013AoG62A146.

Rudjord, Ø., Due Trier, Ø., Zortea, M., Solberg, R., Spreen, G., Gerland, S., Renner, A. and Hughes, N., 2014. Thin ice thickness from MODIS: Improvement of algorithm and evaluation of product. NR Note SAMBA/21/14

Shine, K. P., 1984. Parametrization of the shortwave flux over high albedo surfaces as a

function of cloud thickness and surface albedo. *Quart. J. R. Met. Soc.*, IIO, pp. 747-764

Wang, X., Key, J. R., & Liu, Y., 2010. A thermodynamic model for estimating sea and lake ice thickness with optical satellite data. *J. Geophys. Res*, *115*, C12035.

Yu, Y. and Rothrock, D. A., 1996. Thin ice thickness from satellite imagery. *Journal of Geophysical Research,* 101 (C10), 25753.

4.5 Bremen Sea Ice thickness product

4.5.1 Overview

Sea ice thickness is derived from microwave brightness temperatures measured by the ESA satellite SMOS (Soil Moisture and Ocean Salinity). Sea ice thickness up to 0.5 m (average over one antenna footprint) can be retrieved. If sea ice is thicker than this, it will be recorded as “more than 0.5 metres”. The coverage is daily during the freeze-up season, i.e., October to April in the Arctic and March to September in the Antarctic. SMOS satellite data availability starts in mid-2010. The gridding interval is 12.5 km, while the resolution (antenna footprint size) is 30 to 50 km. The relative error of the retrieved ice thickness is about 30% (Huntemann et al., 2014).

4.5.2 Algorithm description

The L-band radiometer on ESA's Soil Moisture and Ocean Salinity (SMOS) satellite is fully polarimetric, i.e., it measures the four components of the Stokes vector: the intensity *I*, and the polarisation parameters *Q*, *U*, and *V* at a frequency of 1.4 GHz (L band), emitted by the Earth surface (land, sea, ice). The physical basis of retrieving sea ice thickness information from such microwave measurements is (1) the high emissivity of sea ice at L-band as compared to the emissivity of the sea water and (2) the rather large penetration depth of L-band radiation in sea ice (of the order of 0.5 m), thus the L-band emission of sea ice depends on the thickness up to roughly 0.5 m. The algorithm developed at University of Bremen (Huntemann et al., 2014) uses the first two Stokes components, *I* and *Q*, i.e. the average of the vertically and horizontally polarised brightness temperature (usually called intensity) and their difference (the polarisation difference), respectively. Near vertical incidence (0°), the polarisation difference is very small, therefore, data at incident angle between 40° and 50° are used. (Note that an alternative algorithm has been developed at the University of Hamburg, Kaleschke et al. 2012, using only the intensity, *I*, at near-nadir incidence angle.) Comparison with a training data set of ice thickness shows that during the freeze-up period, the intensity is highly correlated with the ice thickness whilst the polarisation difference is anti-correlated, and non-linear functions can be fitted that express intensity *I* and polarisation difference *Q* as functions of ice thickness. The two functions have the general form as follows

$$I_{abc}(x) = a - (a - b) \cdot \exp(-x/c)$$

and

$$Q_{abcd}(x) = (a - b) \cdot \exp(-(x/c)^d) + b$$

Details on the fitted parameters can be found in Huntemann et al, (2014).

From these two functions, a retrieval curve can be constructed in the *I*-*Q*-plane that indicates which pair of (*I*,*Q*) corresponds to which ice thickness (see Figure 18). This way, ice thickness of up to 0.5 m can be retrieved: for a given pair of (*I*,*Q*) the point on the retrieval curve of minimum Euclidian distance is determined. The retrieved ice thickness is then the thickness at that point of the curve.

If the ice is thicker than that, the SMOS signal is saturated, i.e. it does not depend much on the sea ice thickness any more. In this case, the retrieval yields a flag “thickness above 0.5 m”.

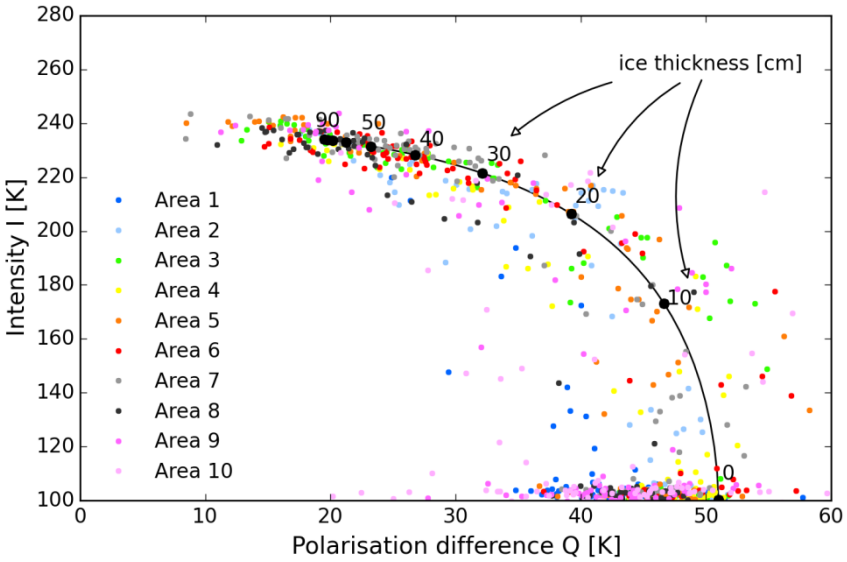

Figure 18. Retrieved curve of sea ice thickness from the Stokes parameters *I* and *Q*. The coloured dots are ice thicknesses in different areas of the training region.

The training data needed to get the retrieval curve had to be derived from modelled sea ice thickness data as in-situ measurements of thin sea ice during the freeze-up period are currently not available. The modelled data are obtained by driving and ice growth model with meteorological reanalysis data from the National Centers of Environmental Predictions (NCEP). The ice growth model chosen was a simple model based on cumulative freezing degree days (CFDD) which is derived from the heat budget equation of sea ice (Weeks, 2010). CFDD is the daily average temperature below the freezing point of sea water (−1.8°C), integrated over the time period since the first sea ice has been formed at this point and in this ice season:

$$\mathrm{SIT\ [cm]} = 1.33 \cdot (\mathrm{CFDD\ [°C]})^{0.58}$$

The ice thickness in the freeze-up season was thus calculated for 10 different locations in the Barents and Kara Sea.

The retrieval agrees well with measurements using helicopter-borne electromagnetic sounding (the EM-bird instrument; Haas 2009) and MODIS thermal imagery retrievals (Mäkynen et al. 2013) – see below. The coverage is daily during the freeze-up season, i.e., October to April in the Arctic and March to September in the Antarctic, starting in mid-2010. The gridding interval is 12.5 km, while the resolution (antenna footprint size) is 30 to 40 km, depending on the position of the footprint in the satellite swath. The relative error of the retrieved ice thickness is about 30%.

In order to retrieve the sea ice thickness, it is helpful to know the sea ice concentration, i.e., the area fraction covered by sea ice. The sea ice concentration is retrieved from the 89 GHz channels (horizontal and vertical polarisation) of the Advanced Microwave Scanning Radiometer 2 (AMSR2) on the Japanese satellite GCOM-W1. The retrieval algorithm, i.e., the ASI algorithm (Spreen et al. 2008), uses the fact that the difference between horizontally and vertically polarised emission from sea ice is much smaller than the polarisation difference of the emission from open water. The spatial

resolution is about 5 km which is the highest resolution for current passive microwave instruments in that frequency range. Both Arctic and Antarctic are covered daily.

4.5.2.1 Input Data Needed

Input data for the sea ice thickness retrieval are either SMOS Level 1C data or SMOS BUFR data (Binary Universal Form for the Representation of meteorological data).

Input data for the auxiliary sea ice concentration are AMSR2 Level 1b brightness temperatures.

4.5.2.2 Processing Chain

In addition to the retrieval algorithm proper, two steps of pre-processing are necessary for the SMOS input data (see Figure 19): Filtering for radio-frequency interference (RFI), and the geometrical conversion of the polarisation parameters from the satellite reference frame to the ground reference frame (XY2HV in the Figure). The RFI filtering makes use of the fact that most RFI causes unphysically high “measurements”: When one pixel has a brightness temperature above 300 K, the whole group of pixels that were acquired simultaneously with that pixel (a so-called snapshot of about 100 by 100 pixels) is discarded.

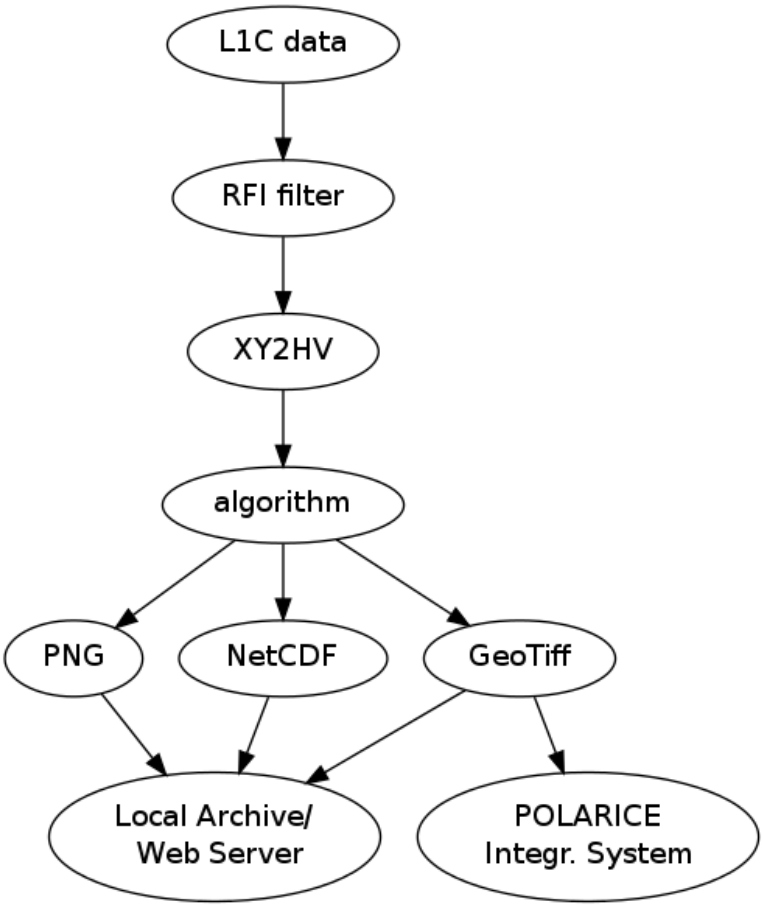

Figure 19. Schematic diagram of the sea ice thickness retrieval algorithm, including the pre-processing steps of RFI filtering and geometrical conversion of the polarization parameters (XY2HV).

4.5.3 Output formats

There are several output data formats in order to meet user needs. They are either maps in image format, for browsing through the data, or gridded data, i.e., quantitative data for further analysis or as input to the user's own mapping and imaging routines.

The map images are in PNG format and show the colour coded sea ice thicknesses on a polar stereographic map including land masses, latitude and longitude grid and a colour legend. (See example maps for Arctic and Antarctic in Figure 20 and Figure 21, respectively).

The gridded data are in GeoTiff format and contain the necessary projection and geolocation parameters, and then the data gridded in polar-stereographic projections commonly used by the National Snow and Ice Data Center (NSIDC), the so-called NSIDC grids for the Arctic and Antarctic, with a grid cell size of 12.5 km. The NSIDC grid for the Arctic is also known as the EPSG projection 3411 (see www.spatialreference.org/ref/epsg/3411), and the one for the Antarctic is EPSG 3412 (www.spatialreference.org/ref/epsg/3412).

The meaning of the data values (1 byte integers):

0	Open water
1 – 50	Ice thickness in cm
51	ice thickness of more than 50 cm
254	No data (e.g. land)

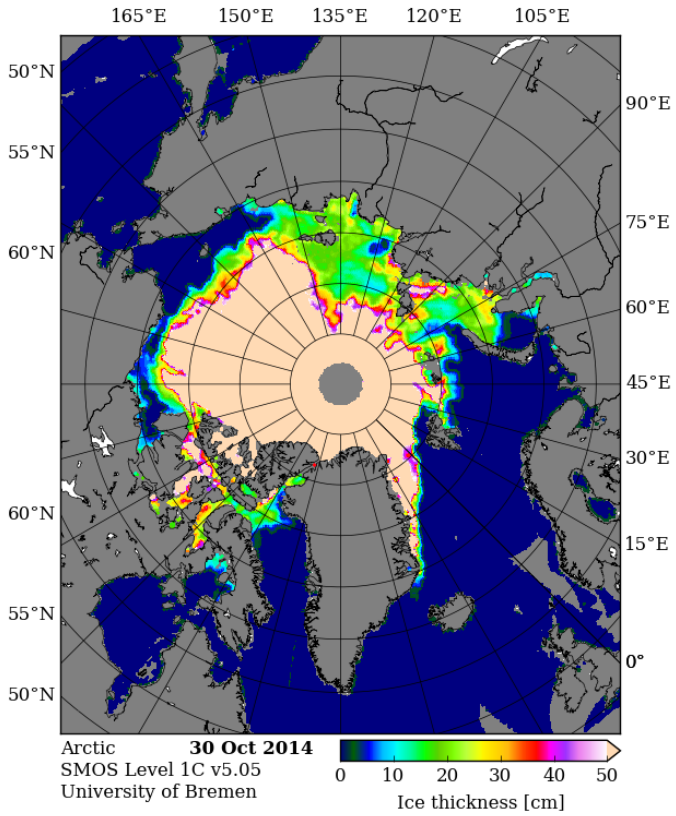

Figure 20. Map of sea ice thickness, Arctic, 30 Oct, 2014, retrieved from SMOS data.

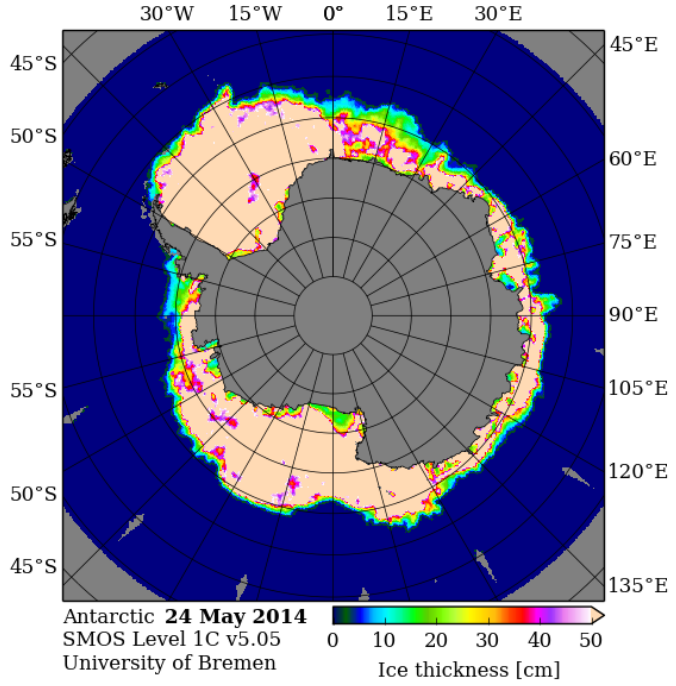

Figure 21. Map of sea ice thickness, Antarctic, 24 May, 2014, retrieved from SMOS data.

4.5.4 Validation, Accuracy

The relative accuracy was assessed to be 30% by comparison of retrieved ice thicknesses with ice thicknesses from the training data described above (Huntemann et al., 2014).

Comparison with sea ice thickness measurements by the airborne EM-bird instrument (one flight over Arctic sea ice yielded good agreement: The correlation is 0.73 and the root mean square (rms) difference is 5 cm (Huntemann et al., 2014). An EM-bird flight over Antarctic sea ice yielded similar results.

Comparison with sea ice thickness retrieved from MODIS yielded good agreement for ice thickness below 20 cm. Above that, ice thickness retrieved from SMOS are generally higher than the comparison data retrieved from MODIS, albeit within the accuracies of both data sets. The correlation is 0.68 and the rms difference from the regression line is 11 cm (Huntemann et al., 2014).

4.5.5 Product summary

Table 7. Summary of properties of the Bremen ice thickness product.

Parameter	Description
Product Description	Thin sea ice thickness based on data from SMOS
Satellite Data	SMOS radiometer data
Sea ice parameter	Thickness of sea ice from 0 to 0.5 m, thicker ice recognised as “thicker than 0.5 m”
Geographical coverage	Arctic and Antarctic
Temporal coverage	As the algorithm depends on non-melting conditions, the temporal coverage is during the freezing season in the respective hemisphere and region. Roughly, this is October to April/May in the Arctic and March to September in the Antarctic.
Spatial resolution	Spatial resolution of the ice thickness data, directly derives from the spatial resolution of the SMOS radiometer which is about 30 to 40 km depending on the position of the pixel in the satellite swath. The ice thickness product, however, is gridded to 12.5 km grid cell (pixel) size.
Temporal resolution	Update interval of the ice thickness chart is once daily, within a few hours of the satellite data acquisition of one complete day.
Delivery time	Thickness data for the previous day ready by about 7:00 UTC
Ice thickness accuracy	Relative error of about 30% for thickness up to 0.5 m. Thicknesses above 0.5 m are recognized as “thicker than 0.5 m”.
Quality information	Accompanying map with the estimated error of each grid point is possible.

4.5.6 References

Haas, C., J. Lobach, S. Hendricks, L. Rabenstein, and A. Pfaffling (2009): Helicopter-borne measurements of sea ice thickness, using a small and lightweight digital EM system, Journal of Applied Geophysics, 67, 234-241, doi:10.1016/j.jappgeo.2008.05.005.

Huntemann, M., G. Heygster, L. Kaleschke, T. Krumpen, M. Mäkynen, and M. Drusch, ”Empirical sea ice thickness retrieval during the freeze-up period from SMOS high incident angle observations,” The Cryosphere, 8, 439–451, 2014, www.the-cryosphere.net/8/439/2014/, doi:10.5194/tc-8-439-2014.

Kaleschke, L., Tian-Kunze, X., Maaß, N., Mäkynen, M., and Drusch, M.: Sea ice thickness retrieval from SMOS brightness temperatures during the Arctic freeze-up period, Geophys. Res. Lett., 39, L05501, doi:10.1029/2012GL050916, 2012.

Mäkynen, M., B. Cheng, and M. Similä, “On the accuracy of the thin ice thickness retrieval using MODIS thermal imagery over the Arctic first year ice,” Ann. Glaciol., vol. 54, no. 62, pp. 87-96, 2013.

Spreen, G., L. Kaleschke, and G. Heygster, “Sea ice remote sensing using AMSR-E 89 GHz channels,” J. Geophys. Res., 113, C02S03, doi:10.1029/2005JC003384, 2008.

Weeks, W.: On Sea Ice, University of Alaska Press, 2010.

5 WP6 - Sea-ice forecasts

5.1 SMHI sea-ice forecast product

5.1.1 Overview

Currently there are a small number of large-scale sea-ice forecast products being provided covering part or the whole of the Arctic Ocean. Examples are:

1. The MyOcean Arctic product which consists of the TOPAZ system run at the Nansen Environmental and Remote Sensing Center using the HYCOM model (http://www.myocean.eu, http://topaz.nersc.no/),
2. The forecasts by the Danish Meteorological Institute running the HYCOM model (http://ocean.dmi.dk/anim/index.uk.php), and
3. The Swedish Polar View forecasts using the HIROMB model run at the Swedish Meteorological and Hydrological Institute (http://www.smhi.se/polarview/).

All these products have one thing in common: the horizontal resolution is coarser than 10 km, and in the TOPAZ case a low temporal resolution (one day) and low data assimilation frequency (weekly). The purpose of the SMHI sea-ice forecast product is to provide a more detailed, high-resolution forecast system for a smaller region, in this case the Nares Strait region, northwest of Greenland; see the map below (Figure 22). Depending on how large the domain will be, it is envisaged that the resolution will be of the order of 500 m.

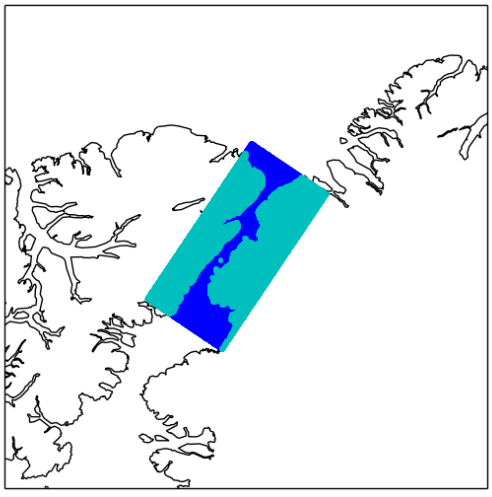

Figure 22. Map showing a possible domain for the planned forecasting system.

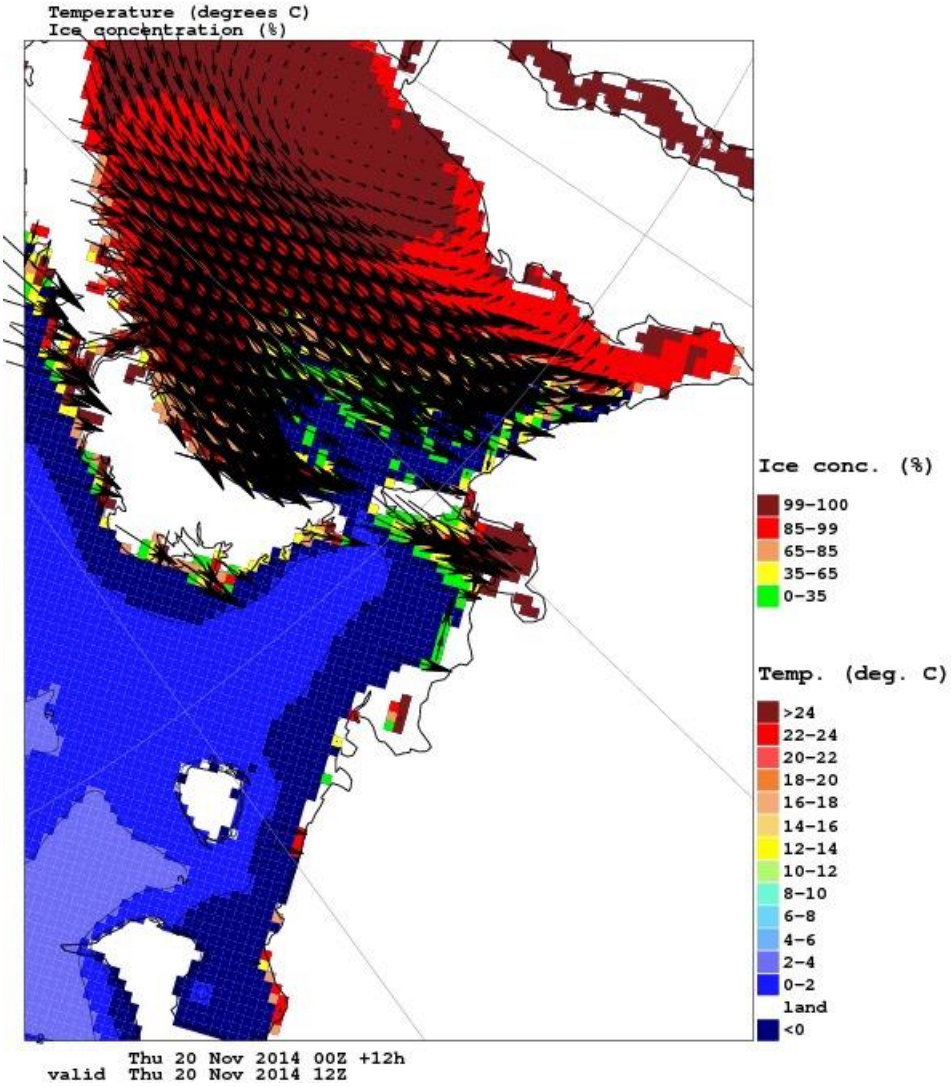

Figure 23. Example of model output, in terms of sea ice concentration, sea ice drift, and sea surface temperature. This example is from a coarse-resolution model (11 km).

5.1.2 Algorithm description

The forecasting model that will be used for the product is NEMO (Nucleus for European Modelling of the Ocean; Madec 2008). It includes a state-of-the-art sea ice model called LIM3 (Vancoppenolle et al. 2012), which has been developed for the Arctic. SMHI have earlier experience from using NEMO in both global and Baltic Sea configurations.

It was planned to use an ensemble method for data assimilation called Ensemble 3D-Var (En3D-Var). It was originally developed for the atmosphere (Liu et al. 2008, 2009) but has recently been implemented at SMHI for sea ice and ocean data assimilation (Axell and Liu, in manuscript, 2014). In addition to the observations and a first guess from a short-range forecast, the Ensemble 3D-Var method requires an ensemble of model states to represent uncertainties in the first guess. The

observations to be used are the OSI-SAF High-Latitude SST (Sea Surface Temperature) and SIC (Sea Ice Concentration) products.

As meteorological forcing it is planned to use meteorological forecast fields from ECMWF (the European Centre for Medium-Range Weather Forecasts). The processing chain can be summarized by Figure 24 below.

Boundary values will be taken from existing course resolution models by interpolating to the higher resolution.

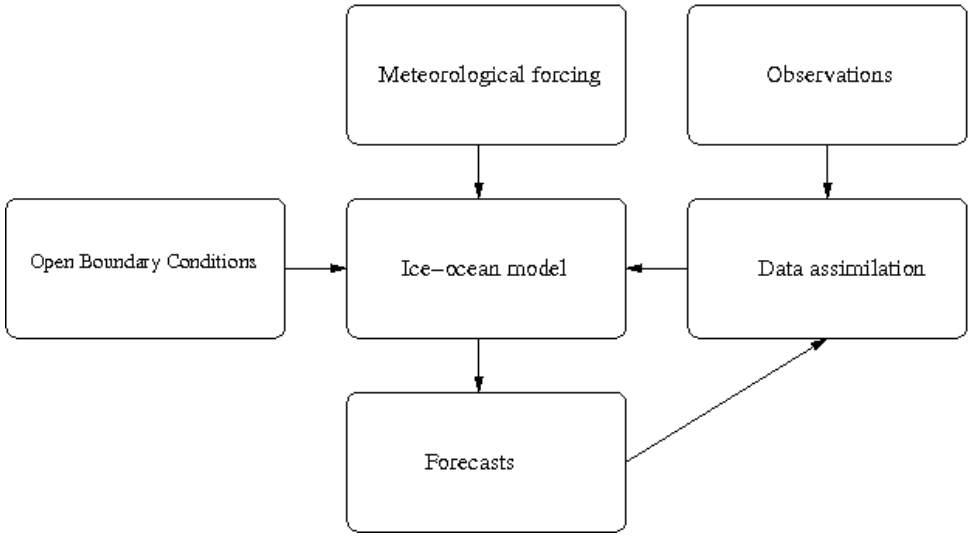

Figure 24. Schematic showing the processing chain of the planned forecasting system.

5.1.3 Output formats

The native output format of NEMO-LIM3 is NetCDF. A large subset of the output data can be obtained for users, as well as updated figures showing the current state of the region of interest. A small subset of the data could be sent directly to ships having small bandwidth. A suitable format for this purpose would be GeoTIFF images. The model will use a rotated lat-lon grid but other projections can be used for images upon end users request.

5.1.4 Validation

The data assimilation system includes automatic collection of error statistics for all assimilated variables. Examples are time series of monthly means of rms errors and bias errors. This type of validation has been used for the reanalysis products as well as for operational products for the Baltic Sea. The statistics can be summarized e.g. on a monthly basis. In addition, it is possible to validate the product visually on day-to-day basis, using an updated web page showing the forecasts. This has been done at SMHI in a Polar View, on an external web page at SMHI (http://www.smhi.se/polarview/). A similar (or the same) web page will be used in this project.

5.1.5 Product summary

Table 8. Summary of the SMHI sea-ice forecast product.

Product description	Ocean and sea ice forecasts based on an ice-ocean model updated with data assimilation.
Ocean circulation model	NEMO (Nucleus for European Modelling of the Ocean)
Sea ice model	LIM3 (the Louvain-la-Neuve sea Ice Model, version 3)
Data assimilation method	Ensemble 3D-Var
Observational input data	OSI-SAF SST and OSI-SAF SIC
Meteorological input data	ECMWF
Output parameters	Ice concentration, total thickness and drift components; Sea Surface Temperature (SST), Sea Surface Salinity (SSS) and Sea Surface Height (SSH).
Coverage	Nares Strait, near Greenland.
Update interval	At least once a day
Spatial resolution	Aiming for 500 m resolution
Delivery time	10 UTC (and possibly 22 UTC)
Formats	NetCDF and GeoTIFF

5.2 DMI Sea-Ice forecast product

5.2.1 Overview

High resolution forecasts of sea ice and ocean currents will improve the safety and efficiency of shipping and offshore operations in ice infested waters. The provision of reliable and accurate sea ice forecasts will facilitate better decision-making at both tactical (e.g. real-time navigation) and strategic (e.g. route planning, risk assessment) levels.

In general ice forecasts are not currently readily available to Arctic navigators. However, POLAR ICE will bring forecasts of ice concentration, ice drift, ice thickness distribution and ice deformation to users for the first time in a unified manner.

POLAR ICE will also provide forecasts at higher spatial and temporal resolutions compared to what is currently available. This greater level of detail will be particularly useful in operational settings when decisions about ship routing and ice management for marine platforms need information about how the sea ice and meteorological conditions will change over the next hours and days.

In order to do so a domain that covers Baffin Bay with a resolution of 2-3 kilometers will be setup and two demonstration periods will be simulated. The current domain suggestion and the resolution can be seen on Figure 25.

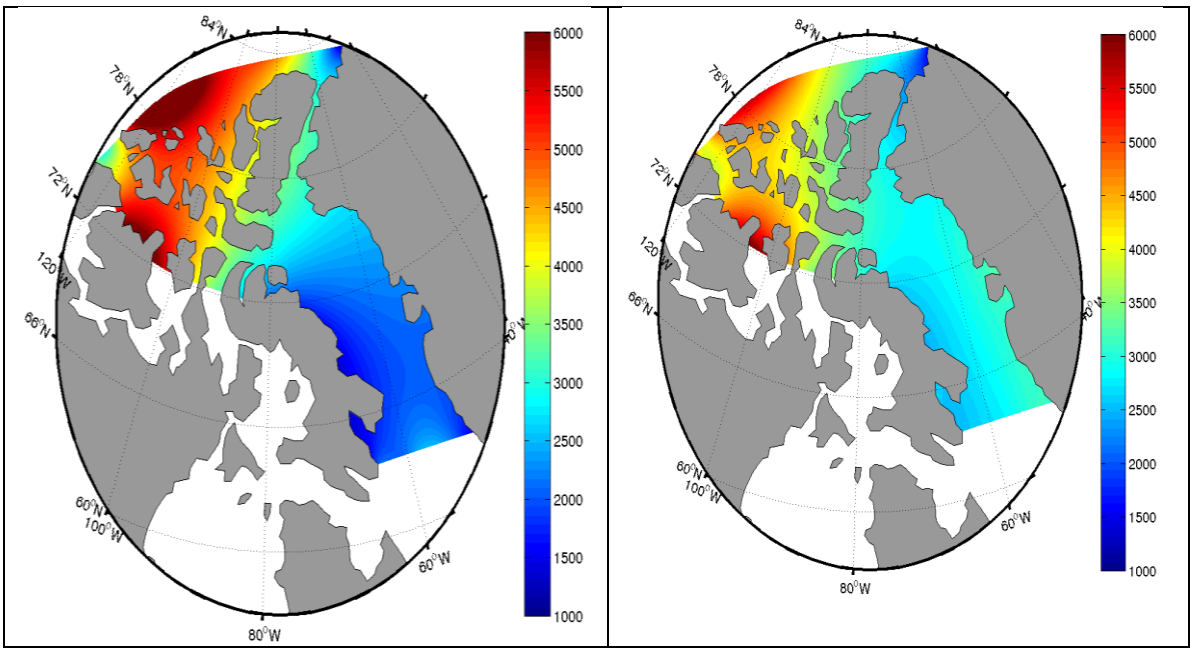

Figure 25. Model resolution dx (left) and dy (right). The colours show the horizontal resolution of the model along the two principal axes in meters. These are not aligned with north and south. Gray areas are land and white areas are not included in the model.

Figure 25 shows that the high resolution has been focused on Baffin Bay as this is the focus area of the demonstration. Parts of the Canadian Archipelago has been included to ease the transition from the Atlantic/North Atlantic model to the regional domain as it is expected that even a slight improvement of the resolution from approximately 10 km to the resolution of the regional model

will improve the transport of heat, salt and sea ice through the narrow straits of the Canadian Archipelago and thus the inflow to Baffin Bay. The reason for not choosing an equidistant grid is that the computational cost increases with the number of points, thus by increasing the number of point the execution time of the forecast will be reduced. By reducing the resolution in the Canadian Archipelago it is enabled to cover a larger area and to represent the Narrow straits with a resolution that is higher than the forecast providing the boundary conditions. The 2d latitudes and longitudes will be provided along with the data set.

This setup will be tested in user defined time periods. Currently it is expected that November 2012 will be used as the first demo phase as the Danish Meteorological Institute had a person on a vessel in Baffin Bay at this time. We will simulate a historical forecast that will show the forecast skill for the given example. The information will then be given to the person who was on board the ship and based on comparisons between observations and model results feedback will be provided. This feedback is intended to describe the quality of the forecast, whether it is the right parameters that have been extracted and at last suggestions to new parameters that describes the sea ice.

5.2.2 Model description

The model to be used is already in operation at the Danish Meteorological Institute (DMI), where it currently runs covering a 10km region of the Arctic/North Atlantic, see Figure 26.

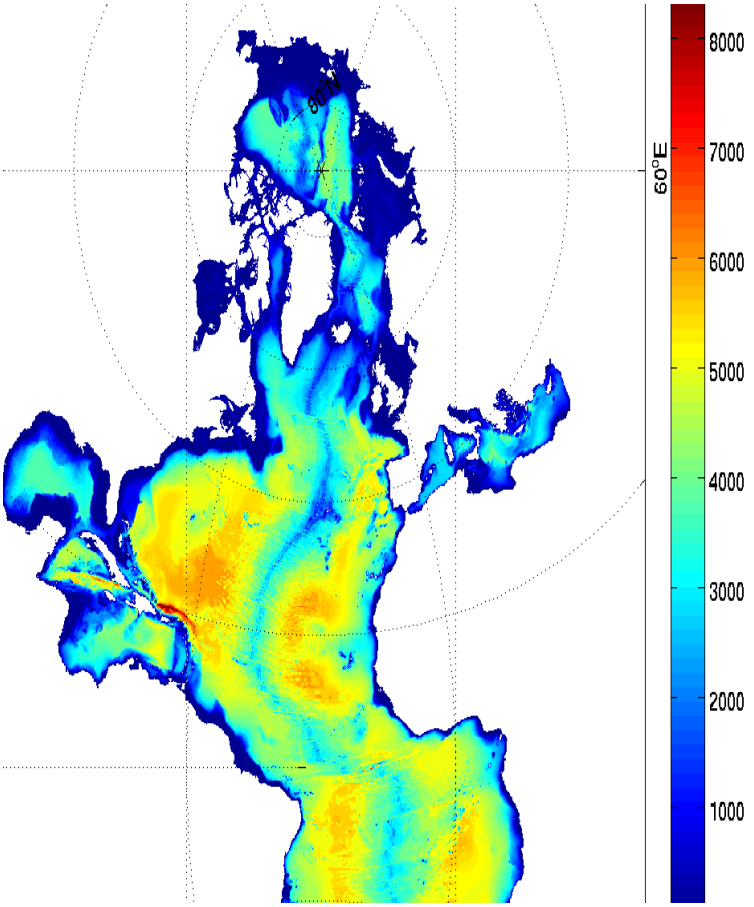

Figure 26. Bathymetry of 10km operational system. Colour scale indicates depth of model.

This model runs operationally twice a day at DMI and provides a 5 day forecast with output every hour. Forecast parameters include (but are not limited to) ice concentration, ice thickness and ice velocities as well as ocean currents, ocean temperature and salinity. This setup will be used as boundary conditions for the high resolution Baffin Bay model currently being implemented.

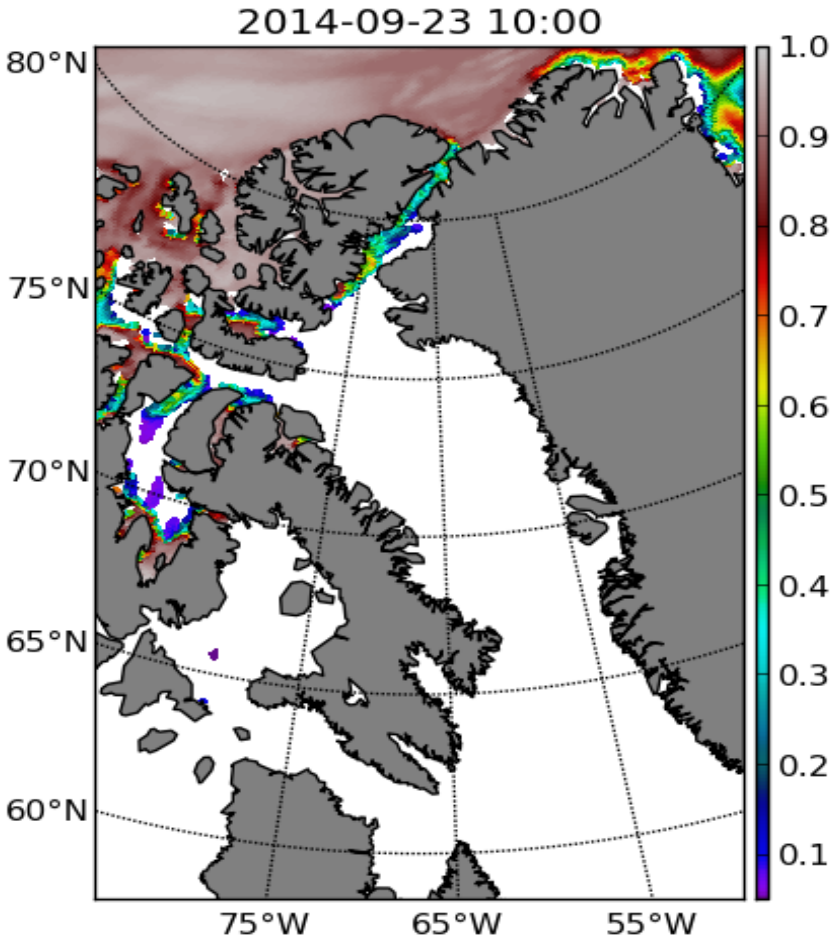

Figure 27. Example of operational forecast from coarse resolution model (10km). Area correspond to focus are. Color scale represents sea ice concentration. Gray is land. White is ocean.

The coupled ocean and sea ice model is a slightly modified version of HYCOM (HYbrid Coordinate Ocean Model) v2.2.55 [Bleck, 2002, Chassignet *et al.*, 2007] and CICE v4.0 (Community Ice COde) [Hunke and Dukowicz, 1997] coupled with ESMF (Earth System Modeling Framework) [Collins et al., 2005].

HYCOM is a 3D ocean model which explores a hybrid coordinate that is isopycnal in the open, stratified ocean, but smoothly reverts to a terrain-following coordinate in shallow coastal regions, and to z-level coordinates in the mixed layer and/or unstratified seas. The vertical mixing is governed by the KPP scheme [Large 1994].

CICE is a dynamic and thermodynamic sea ice model that applies an elastic-viscous-plastic (EVP) sea ice rheology and includes a multi-category sea ice thickness distribution. ESMF exchanges surface parameters between HYCOM and CICE. The following parameters are exchanged (Table 9).

Table 9. The surface parameters exchanged between the HYCOM and CICE models.

HYCOM to CICE	*CICE to HYCOM*
Mixed layer temperature	Sea ice concentration
Salinity of mixed layer	Sea ice thickness
Velocities along model grid in both principle axis	Solar heat flux through ice into ocean
Sea surface height	Ice freeze/melt heat flux
Heat flux from ocean to ice	Ice freeze/melt salt flux
Mixed layer thickness	Sea ice velocity along two principle axis.
	Sea ice temperature

A nudging scheme has been implemented in order to assimilate observations into the system. Sea surface temperatures are assimilated as a heat flux according to:

$$Flux_{sst} = \alpha * (sst_{obs} - sst_{mod}) * c\_w \quad (1)$$

C_w is the heat capacity of water. α is a weight factor and c_w is the heat capacity of sea water. The energy flux is positive towards the ocean.

Assimilation of sea ice is defined based on the following equation

$$Con_{new} = \beta * Con\_mod + (1 - \beta) Con\_obs \quad (2)$$

Con_{new} is the sea ice concentration after assimilation. Con_{mod} and Con_{obs} are the modeled and the observed sea ice concentration before the assimilation. β is the weight factor.

5.2.3 Input data

The regional model expects input from the boundaries and atmospheric forcing. The atmospheric forcing consists of the following parameters:

- Wind speed and direction 10 meters above water level
- Air temperature 2 meters above sea level
- Humidity
- Precipitation
- Incoming long wave radiation
- Short wave incoming radiation

The heat budget at the surface is calculated as the sum of the long and short wave radiation reduced by reflected radiation at the surface plus sensitive and the latent heat. The precipitation acts as a fresh water flux at the surface.

The assimilation of sea ice and sea surface temperatures requires 2d fields of SST and sea ice concentration. In addition a relaxation towards climatology of salinity is used. This is justified by the relatively large uncertainty of the freshwater input from rivers and glaciers.

The boundary conditions are defined by the operational system at DMI. They provide barotropic and baroclinic currents, ocean temperatures, salinity, sea ice concentration and sea thickness. The plan is to incorporate sea ice velocities as well.

5.2.4 Process chain

The model system depends on the following process chain.

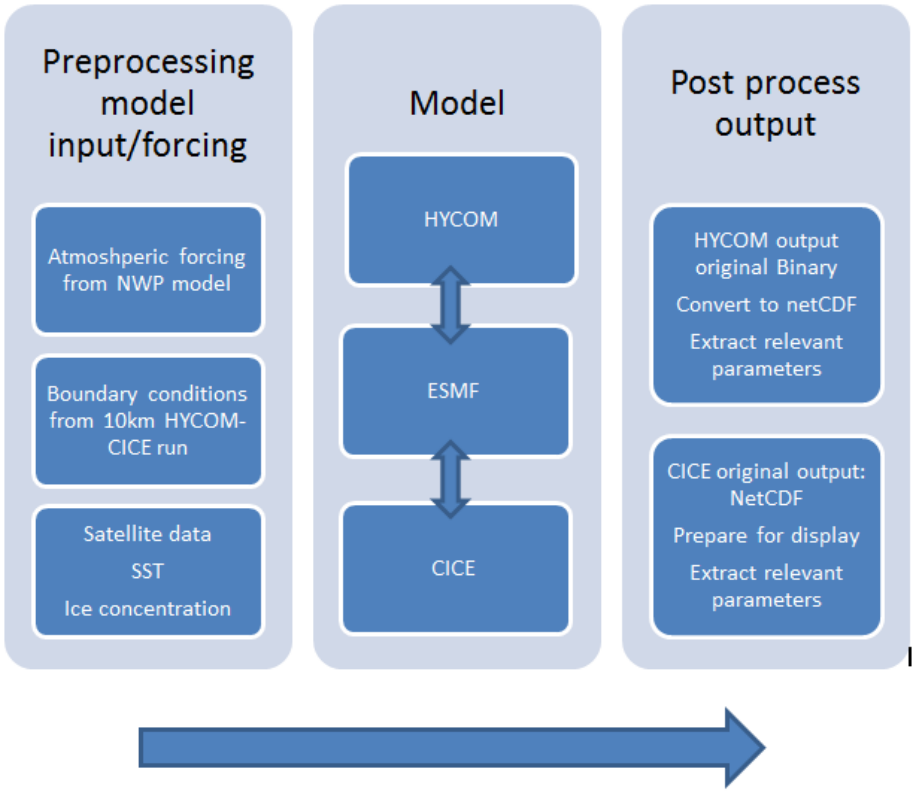

Figure 28. The DMI ice-forecast processing chain.

5.2.5 Output formats

Output will be displayed on the POLAR ice platform and/or seaice.dk. In addition to this data will be made available as either binary or netCDF files depending on the requirements from users. Table 10 describes the suggested output parameters.

5.2.6 Validation

The sea ice of the regional model of Baffin Bay will be validated based on a range of model output, ice charts automated ice products etc. Focus will be on the sea ice extend and sea ice thickness from SMOS. Ocean parameters will include validation of currents, sea surface temperatures and salinity where observations are available. In addition the skill of the regional model will be compared to the skill of the coarse resolution model in order to demonstrate that the increase of resolution increases

the skill. Main focus will be on the upper part of the ocean as this is what is important for ship routing.

5.2.7 Product summary

The final product will be dependent on feedback from the demonstrations, however, an initial list of outputs can be seen in Table 10.

Table 10. Product summary: output parameters and resolution.

Area	**Baffin Bay**
Spatial resolution	~2 km
Temporal resolution	1 hour
Ocean	
Output at depths	1.5, 4.5, 8, 14, 20, 30 and 50 [m]
Parameters	Temperature [°C] Salinity Currents: Northward and Eastward [m/s]
Sea Ice	
Parameters	Concentration [%] Thickness [m] Pressure/strength Divergence Velocities Northward & Eastward [m/s]

5.2.8 References

Bleck, R. (2002). An oceanic general circulation model framed in a hybrid isopycnal-Cartesian coordinates. Ocean Modelling, 37, pp. 55-88.

Chassignet E.P, Hurlburt H.E., Smedstad O.M., Halliwel G.R., Hogan, P.J., Wallcraft A.J., Baraille R. and Bleck R. (2007). The HYCOM (Hybrid Coordinate Ocean Model) data assimilative system. J. of Mar. Sys. 65, pp. 60-83

Collins, N., G. Theurich, C. DeLuca, M. Suarez, A. Trayanov, V. Balaji, P. Li, W. Yang, C. Hill, and A. da Silva (2005). Design and Implementation of Components in the Earth System Modeling Framework. International Journal of High Performance Computing Applications, Volume 19, Number 3, pp. 341-350.

Hunke, E. C. and Dukowicz, J (1997). An elastic-viscous plastic model for sea ice dynamics. J. Phys. Oceanography. 27: 1849-1867

Large, W. G., J. C. McWilliams, and S. C. Doney, 1994: Oceanic vertical mixing: a review and a model with a nonlocal boundary layer parameterization. Rev. Geophys., 32, 363-403.

6 WP7 - Transition to Sentinel

6.1 Sentinel-1 compressed information product

6.1.1 Overview

6.1.1.1 Requirements review

The results from the end user consultation phase of the POLAR ICE project revealed that there is a significant requirement for SAR data to be provided as a product, in addition to the more value-added products that are being developed within POLAR ICE, e.g. sea-ice pressure ice thickness and ice forecasts. Eleven of the twenty two end users contacted expressed an interest in SAR data. End users can obtain a lot of useful information in SAR imagery that is not necessarily communicated in ice charts, which only convey the average ice conditions over relatively large regions and don't contain information about the specific locations of smaller scale ice features such as ice ridging and icebergs.

The successful launch and commissioning ESA's Sentinel-1 satellite offers a new opportunity for providing SAR imagery to end users in polar waters. However, there remains a significant challenge in getting SAR data out to vessels because of their large data volumes. A single typical Sentinel-1 Extra Wide mode (EW) image is ~550 MB, indicating that a significant degree of compression is required if products of this size are to be delivered on a regular basis to vessels at sea. Image compression is a topic that has received considerable research and development attention over recent decades. Most image compression techniques work by reducing the high spatial frequency components from an image, leaving less data to be communicated, while retaining the main overall elements of the image which are present in the lower frequency components. This approach is used for example in the JPEG and JPEG-2000 formats, which use the discrete cosine transform and wavelet transform respectively at the core of their algorithms.

In addition, SAR images are often reduced in volume simply by averaging pixels together to form a smaller image. However, the problem with removing high frequency spatial components is that these often contain information that might be useful to end users. In general, the overall distribution of ice floes will be maintained by compression techniques, but features such as ice-ridging, small ice floes and icebergs will often be degraded or lost completely in a low data volume product. In the end user consultation phase six end users expressed an interest in improved ice ridging information and seven in improved iceberg information.

6.1.1.2 Product overview

A product has been developed which aims to allow the high spatial frequency components to be communicated, if they are required, as well as the low frequency components. This is achieved by separating the original image into two components, one containing the low frequency information and the other the high frequency information.

The low frequency image uses the same principles that are used ordinarily in image compression, i.e. initial smoothing and downsizing of the image, followed by a standard compression technique. In addition, the final low frequency output product is transmitted in a GEOTIFF format, so that it can be displayed within the POLAR ICE viewing systems.

In order to create the high frequency image the high spatial frequency components within the SAR image are extracted using a point target detection algorithm and a linear feature detection algorithm. The resultant information is finally stored in the Shapefile format, so this can be displayed in conjunction with the low frequency image if required.

6.1.2 Algorithm description

Figure 29 provides a schematic diagram illustrating the main stages of the algorithm. It can be seen that the initial Sentinel-1 image enters two parallel processing chains: (1) the low spatial frequency stages (indicated by the numbered "L" labels) and (2), the high spatial frequency stages (indicated by the numbered "H" labels). Two output products are produced at the end.

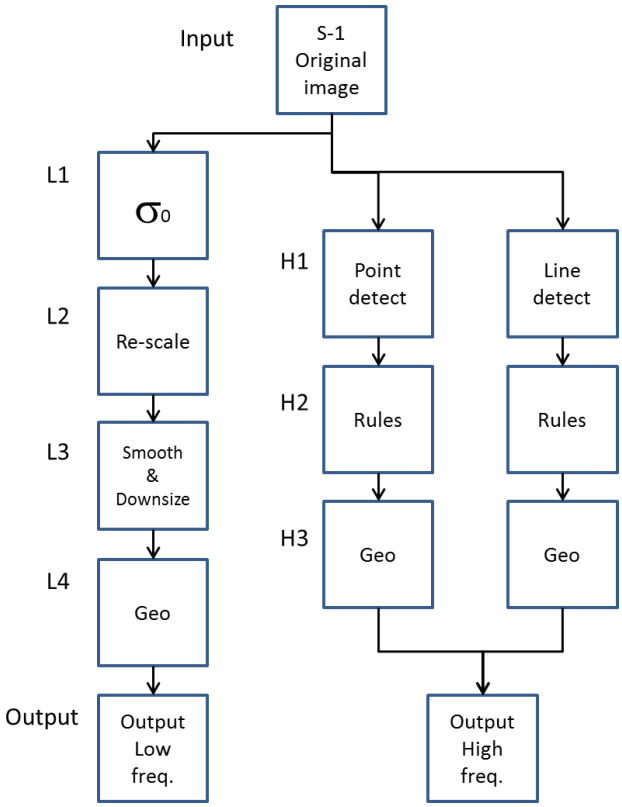

Figure 29. Schematic algorithm overview.

Considering each stage of the algorithm in more detail:

Input: the algorithm only requires one input, which is Sentinel-1 image data. To-date the algorithm has been tested on Extra Wide mode (EW) data, but the overall algorithm would be equally applicable to other Sentinel-1 modes, including those with different polarimetric channels.

In the algorithm that has been tested to date, the algorithm has used an initial step before passing into the low- and high-spatial stages whereby the image is divided into nine approximately equally sized sub-images on a 3x3 grid. If the end user is only interested in a specific region this would allow them to select the relevant region or regions, thereby omitting unnecessary date transfer.

L1 Sigma naught: The Sentinel-1 image data values are converted to backscatter sigma naught values. Backscatter refers to the ratio between the scattered and incident powers. The sigma naught backscatter coefficient is given when this value is normalized by a standard area, as measured on the ground.

There are two reasons here for converting to sigma naught: (1) to remove some of the across range variation in backscattered intensity, (2) to work out the radiometric range that is appropriate to consider for conveying sea ice information, which is considered in L2.

The pixel values in a Sentinel-1 image represent the backscattered amplitude signal and are stored as 16 bit integers. This allows a very wide range of targets with widely different brightness values to be measured, ranging from relatively dark targets such as sea ice, which might have backscatter sigma naught values of -10 dB (e.g. for multi-year ice at C-Band), to urban and industrial scenes which might have backscatter values of +20 dB, i.e. ~1,000 times brighter in intensity.

Image pixel values can be converted to sigma naught values by using a Look-Up table present in the Sentinel-1 header file (see Figure 30).

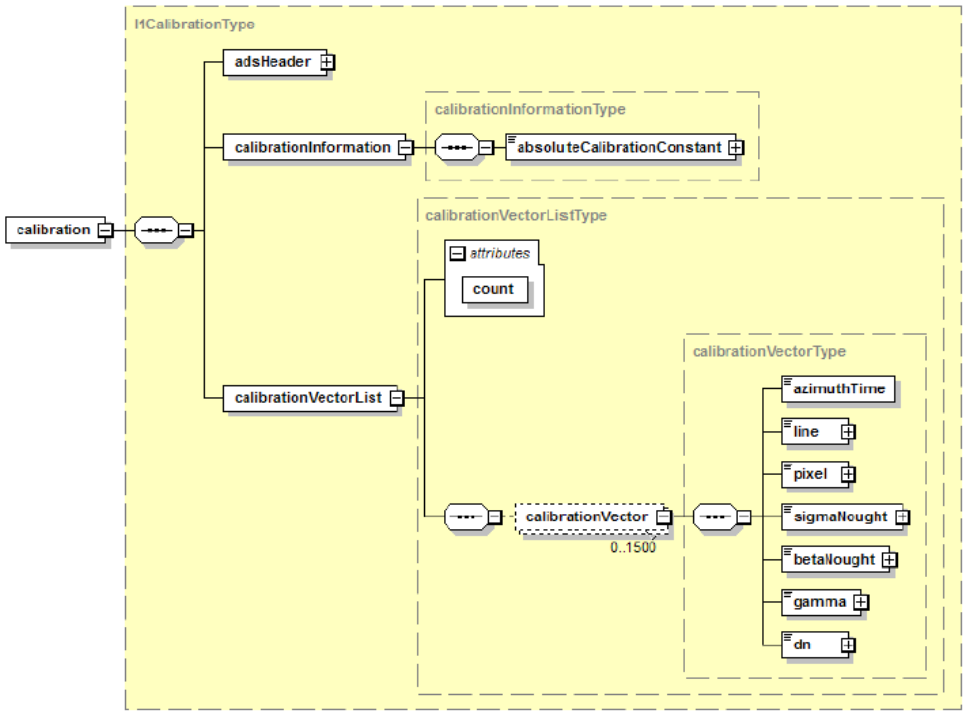

Figure 30. L1 Calibration Data Set, showing where the Sigma Naught look up table resides.

L2 Rescale: The Sentinel-1 amplitude data is stored as 16 bit integers. Only a small range of this is applicable for ice and ocean applications. In general the range between -30 dB and 0 dB covers all the likely backscatter values for sea ice and its ocean background. Some young ice types and very calm ocean might have lower backscatter values than this, but -30 dB is the approximate noise floor of the instrument, meaning that targets with signatures below this will be raised to this “floor” level by the system noise in the sensor. At the higher end of this range, very high sea states and

backscatter from icebergs might be greater than 0 dB, but this is not a problem since point targets such as icebergs are being identified separately in a processing chain which does not include the rescaling process. Figure 31 provides a schematic illustration of the rescaling process.

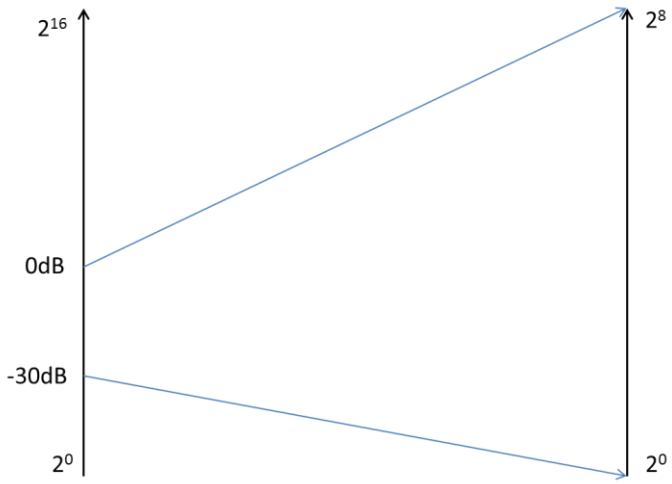

Figure 31. Schematic diagram, showing how the radiometric range of the Sentinel-1 data useful for ice information is mapped from a 16 bit input range to an 8 bit output range.

L3 Smooth and downscale: The simplest way to reduce the size of the output image is to average and down-sample the image. This provides an image with fewer pixels to transmit and also reduces the speckle noise in the data, which makes the image more amenable to being compressed further by e.g. the JPEG format. A smoothing algorithm can also be used as a part of this process, to further reduce the small scale variation in the data, bearing in mind that the smallest ice features will be retained by the separate high frequency image. The smoothing process adopted in the algorithm uses a series of median and Gaussian filters to create a form of ice feature segmentation.

L4 Geo & Output: The output image is converted into the GeoTiff format so that it can be read into visualization systems and displayed in its correct geographical context.

H1 Point/Line detect: Two separate algorithms are used (1) to detect point features (2) to detect linear features.

The point feature algorithm is based on a ship detection algorithm which was developed as a part of the Nereids FP7 project concerning maritime surveillance, which ran between 2010 and 2014. The algorithm makes use of a median filter to isolate genuine bright targets rather than speckle noise and links bright pixels together into groups to form larger targets.

The line detection algorithm is based on a Canny edge detector, on the basis that the linear features in an ice image will also present an edge on each of its sides.

H2 Rules: On both the point and linear feature detected images, a set of morphological rules are applied to consolidate the point and linear targets, e.g. filling holes within targets and reducing the thickness of the linear features to just one pixel in width.

H3 Geo & Output: The output image is converted into the Shapefile format, so this can be displayed in the POLAR ICE visualization systems.

6.1.3 Validation

The other products being developed and provided as a part of the POLAR ICE project are based on previous products which have a heritage of past validation. In contrast; because the compressed sea-ice Sentiel-1 information product is new, the validation to-date has consisted of in-house analysis of the output.

Figure 32 shows an example image that has been analysed, which is an Extra Wide Sentinel-1 image acquired on the 3rd October 2014 close to the Antarctic Peninsula (the image is the Quick-Look product which comes with the main Sentinel-1 product). Figure 33 shows the central subsection (of the 9) from Figure 32 without any smoothing or down-sampling.

Figure 34 shows a smoothed version of the central sub-image portion from Figure 33, but with the point target features highlighted. Figure 35 shows just the point target features in the output Shapefile from the central portion of the image, which are displayed in the Quantum GIS system. Figure 36 shows the full Sentinel-1 high-spatial frequency Shapefile image in the Quantum GIS system.

Investigations regarding the compression rates possible are ongoing.

Figure 32. Sentinel-1 Quick-Look image:
S1A_EW_GRDH_1SSH_20141003T075216_20141003T075316_002662_002F70_6670.

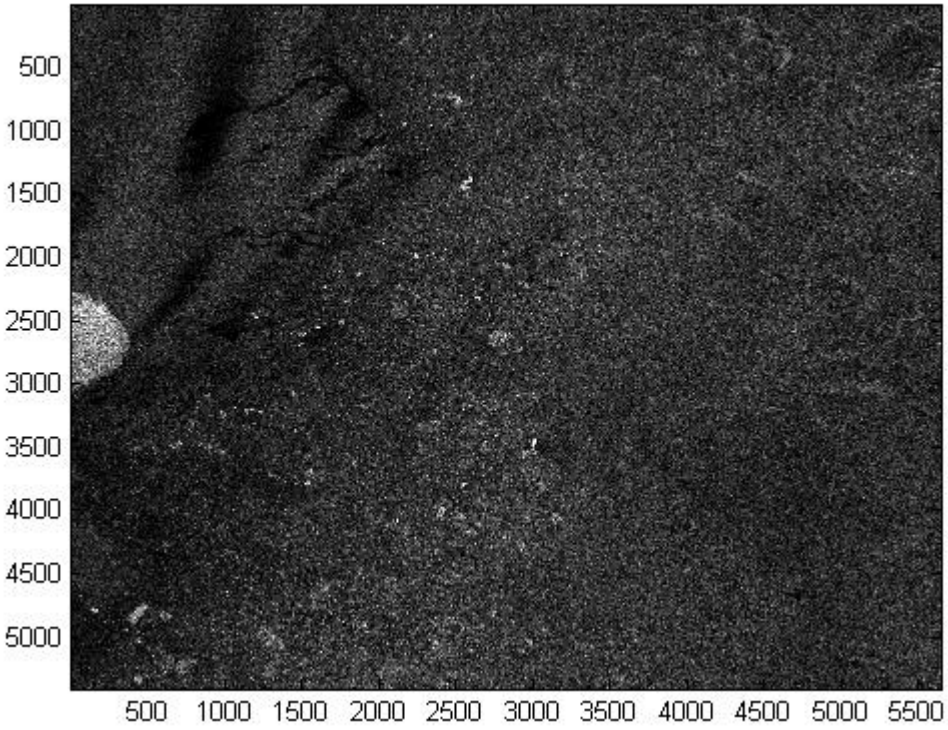

Figure 33. Central sub-image portion of the Sentinel-1 Quick-Look image shown in Figure 32.

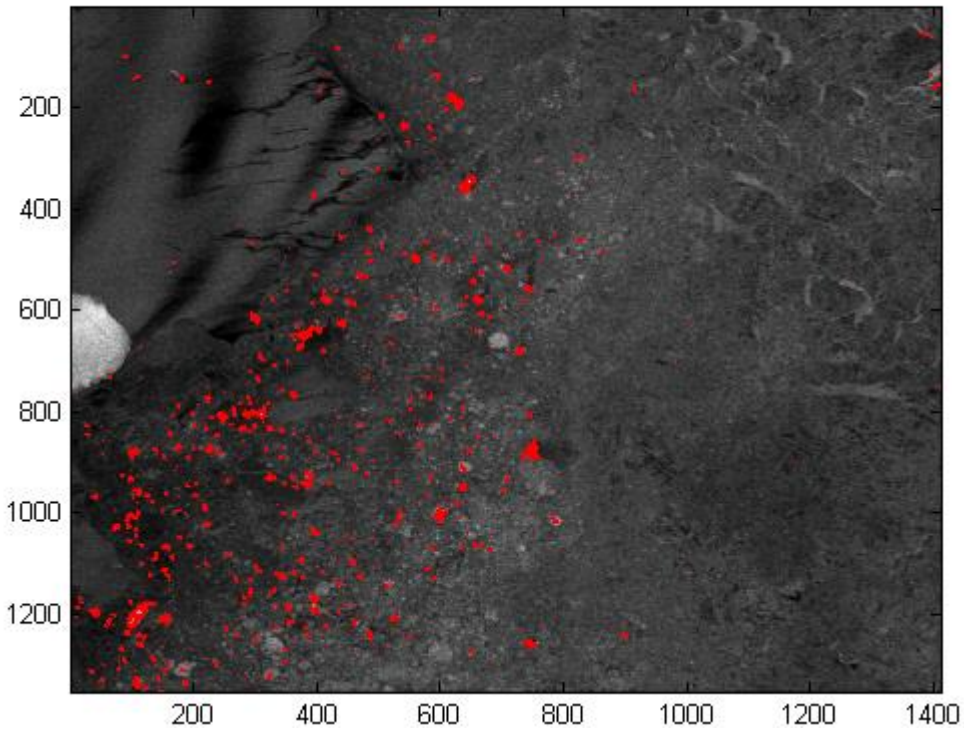

Figure 34. Smoothed version of the central sub-image portion from Figure 33, with the point target features highlighted.

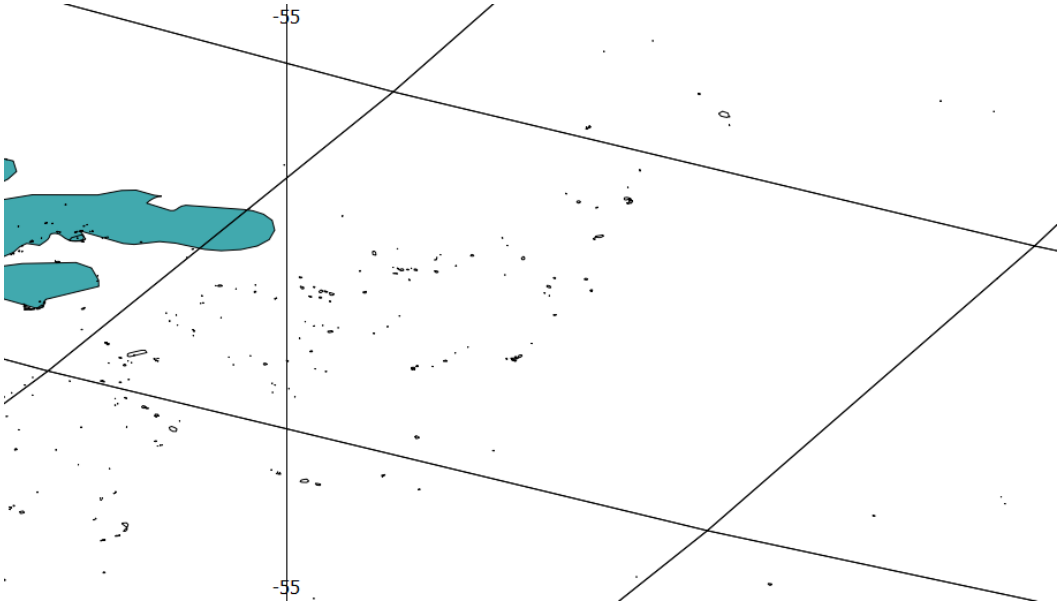

Figure 35. The Shapefile data showing the point target features (from the data also shown in Figure 34) using the QGIS system.

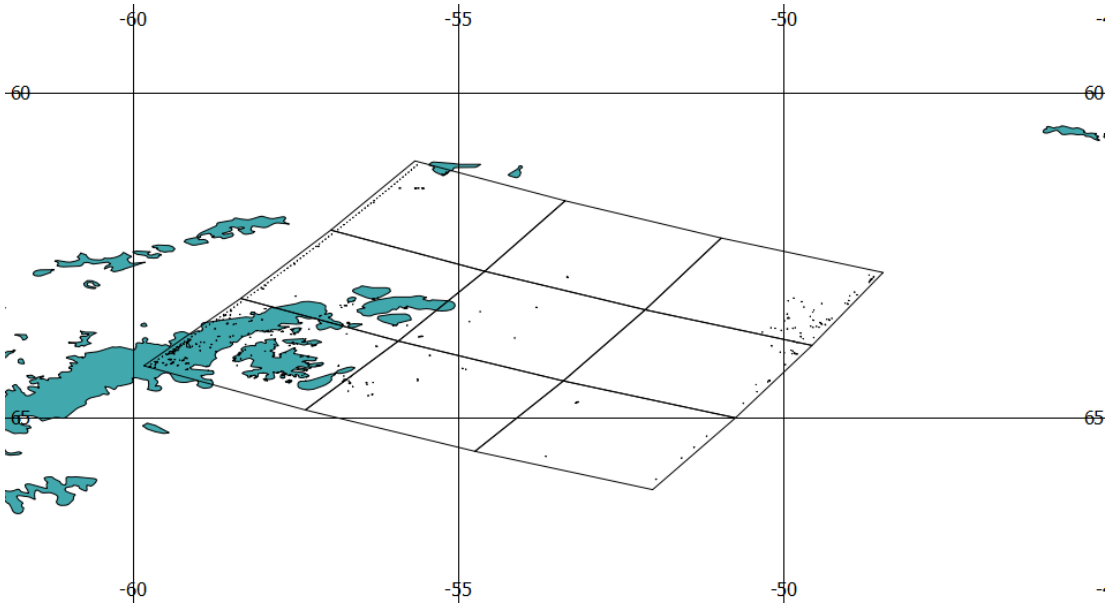

Figure 36. The Shapefile data showing the point target features for the full Antarctic Peninsula Sentinel-1 image data.

6.1.4 Product summary

Table 11. Summary of the Sentinel-1 compressed information product.

Product description	Compressed Sentinel-1 image products suitable for downloading by vessels. The product consisting of two images (1) containing the aggregate low-spatial frequency components of the original image and (2) which contains the higher frequency components of interest, namely point and linear features, but not the unwanted SAR speckle.
Satellite input data	Sentinal-1 image data.
Sea ice parameter(s)	(1) A low resolution version of the Sentinel-1 image. (2) Point and linear features; icebergs, ice ridges, the outline of ice floes.
Coverage	To be determined, but in principle any Arctic and Antarctic regions.
Update interval	As frequently as the Sentinel-1 data is updated.
Spatial resolution	1 km
Delivery time	To be determined.
Formats	GeoTIFF-image, Shapefile.

6.2 Iceberg product

6.2.1 Overview

The iceberg detection service supports safe shipping and offshore drilling operations by providing near real-time detection of icebergs based on satellite synthetic aperture radar (SAR) imagery. The iceberg detection product provides location information about icebergs detected in single and dual polarisation SAR imagery. Iceberg position information is provided in latitude/longitude coordinates. In addition to position, the product contains iceberg attribute information extracted from the SAR image such as length, width, area, sigma nought pixel brightness and variance.

6.2.2 Algorithm description

A series of algorithms are implemented within the Iceberg Detection Software in order to produce an iceberg detection product as shown in Figure 37. The iceberg detection software performs sigma-nought calibration to SAR data. A Constant False Alarm Rate (CFAR) adaptive threshold detection algorithm is applied to the calibrated SAR data to produce detection results. Ship/iceberg discrimination algorithms have been developed based on a quadratic discriminant algorithm and are applied to each detected target. Discrimination algorithms are available for specific SAR satellite beam modes for single and dual polarization data.

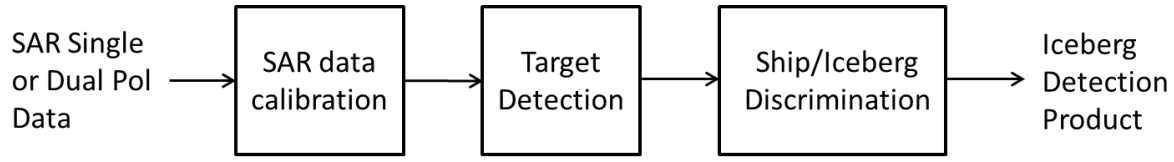

Figure 37 Algorithm flowchart.

The algorithms require the native SAR data as input. SAR data types accepted included RADARSAT-1, RADARSAT-2, ENVISAT, TerraSAR-X, COSMO-SkyMed and Sentinel-1. Other information is required from the algorithm operator such as the constant false alarm and SAR polarization for processing.

SAR data is acquired in real-time for operational use or historical archive if the system is being used to conduct a survey of iceberg behaviour. It is downloaded and catalogued through the C-CORE order desk. An analyst uses the Iceberg Detection Manager (IDM) to define the parameters for the Iceberg Detection Software (IDS). The analyst runs the IDS through the IDM interface to produce an initial iceberg detection product. This product undergoes a manual quality control procedure to assist in eliminating false alarms. A final product is produced by the IDM in a custom format such as a text file, MANICE, shape file or an ICEMAR compatible product. This process is illustrated in Figure 38.

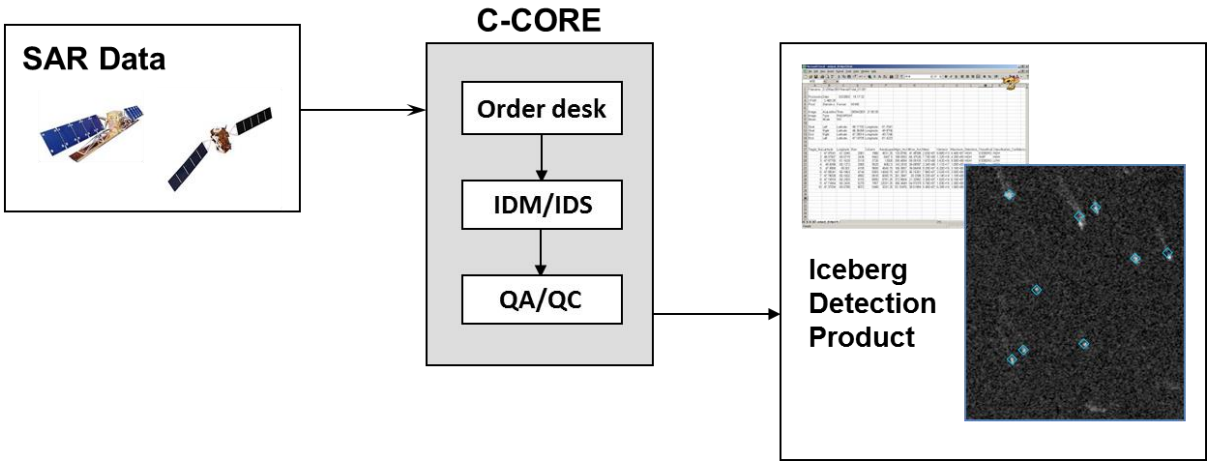

Figure 38 Iceberg Detection Process.

6.2.3 Output formats

The following output products are available:

- Text file – a tabular detection report containing information for each detected target. This information includes a target ID, target location (lat/long), target area, detection confidence, classification and other descriptive features.
- Shape file – a geospatial vector data format containing a point for each detected target. Each target has attribute information which includes a target ID, target area, detection confidence, classification and other descriptive features. An example of a SAR image with annotated icebergs is shown in Figure 39. Figure 40 shows the detections as a geospatial vector displayed on a georeferenced map.
- MANICE file – product following the Manual of Standard Procedures for Observing and Reporting Ice Conditions as defined by Environment Canada as shown in Figure 41.
- ICEMAR product – ICEMAR product containing a provider capability XML document and an IMZ file containing a provider product metadata XML document and the product shape files.

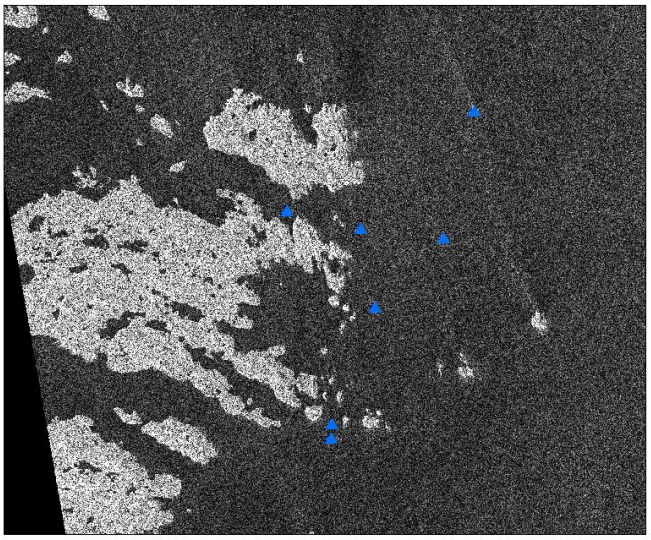

Figure 39 SAR Image annotated with Iceberg Detections.

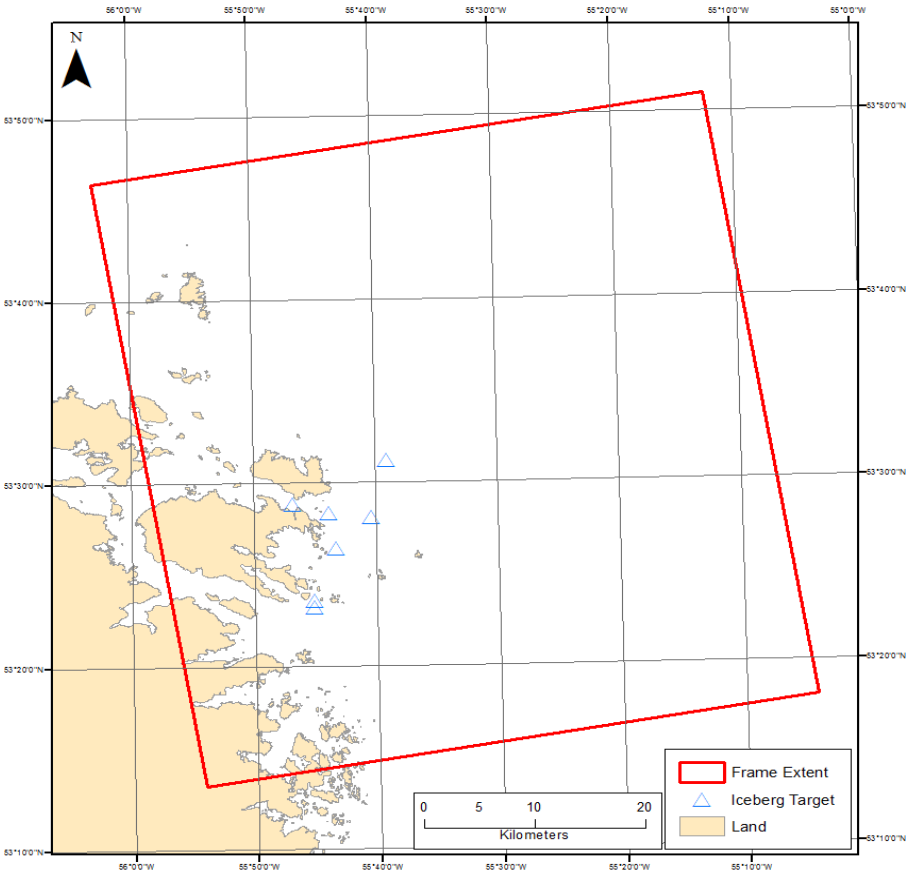

Figure 40 Iceberg Detections Viewed as a Geospatial Layer.

```
IBCN3 CORE 101340
RSA2 70069 080712
00000
75349 05538 Z2137 1XXXX 2XXXX 3015015 4XXXX
75316 05529 Z2138
11111
62137 53232 55452 01X60 14220 24076
62137 53236 55452 01X40 14090 24059
62137 53264 55433 01X60 14237 24047
62137 53281 55404 01X60 14243 24109
62137 53284 55438 01X50 14131 24080
62137 53288 55468 01X40 14084 24046
62137 53312 55391 01X60 14242 24174
55555
REMARKS
This message was generated automatically for the Canadian Ice Service using the target detection system.
Run Time:   2012-Jul-10 15:54:28
Input Data File: C:\ICEBERG\911_working\20120708\213752\product.xml
Input Data Type: RADARSAT-2
Image Acquisition Time:   2012-Jul-08 21:37:52
Beam Mode: F4
CFAR Parameter:  15.00 Standard Deviations
Total Number of Targets: 7
Number of Icebergs: 7
Number of Ships: 0
Number of Unknown targets: 0
POD Small = 84%
POD Medium = 93%
POD Large = 100%
Extracted Wind Speed = N/A
Start Left Point:  53.773490 -56.050808
Start Right Point:  53.849717 -55.205597
End Right Point:  53.300579 -55.068741
End Left Point:  53.224305 -55.902920
Operator noted conditions and comments:
Clutter: LOW TO MODERATE
Atmospheric conditions: LOW
Sea ice: NONE
Image area analyzed: FULL
Land mask: NTS 1:50,000 BUFFERED 125 METERS
Other comments on image quality: GOOD IMAGE
END
```

Figure 41 Iceberg Detection in MANICE File Format.

6.2.4 Validation

The detection of icebergs depends on image spatial resolution and viewing geometry, iceberg shape and sea state. Under typical conditions, the probability of detection for small icebergs (waterline length 15 to 60 m) is at least 70% and frequently approaches 100% for larger icebergs. Probability of detection statistics derived from 30 m resolution C-Band HH polarization SAR data are shown in Figure 42 through Figure 44 [1]. These statistics were developed for Small, Medium and Large size icebergs as defined by Environment Canada Iceberg Code which are defined based on waterline length and height. Statistics specific to Sentinel-1 will be accumulated as part of the POLAR ICE program.

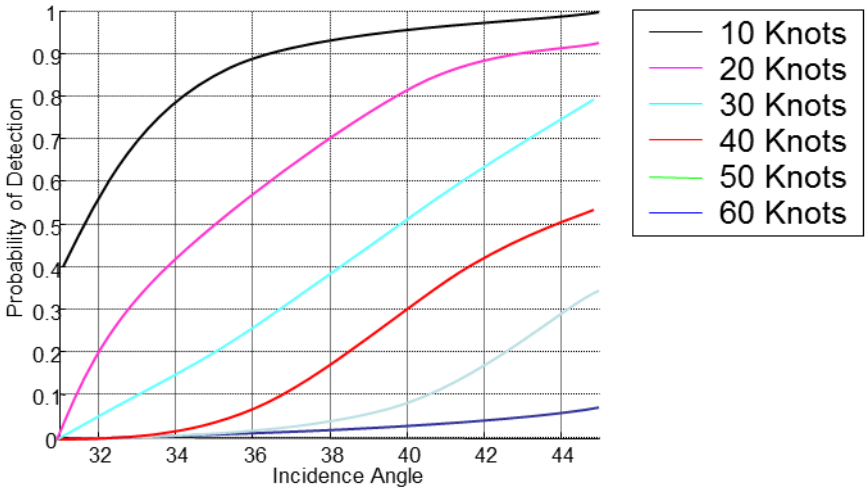

Figure 42 Probability of Detection for Small Icebergs.

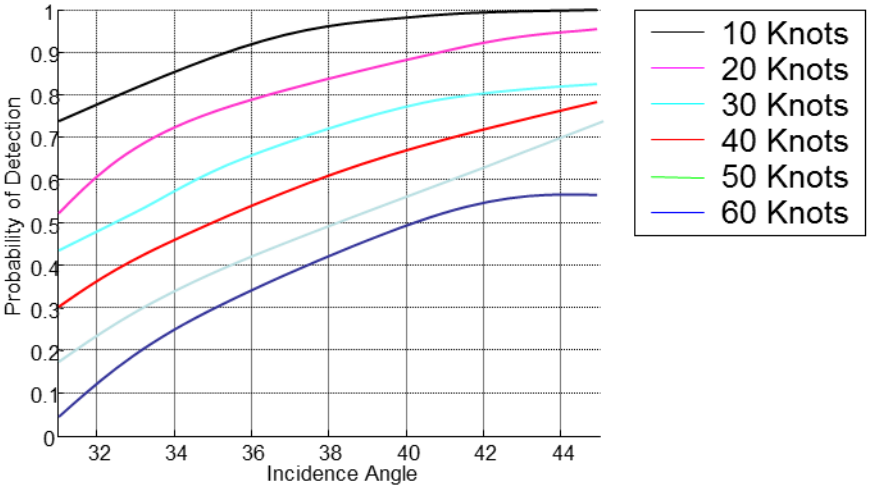

Figure 43 Probability of Detection for Medium Icebergs.

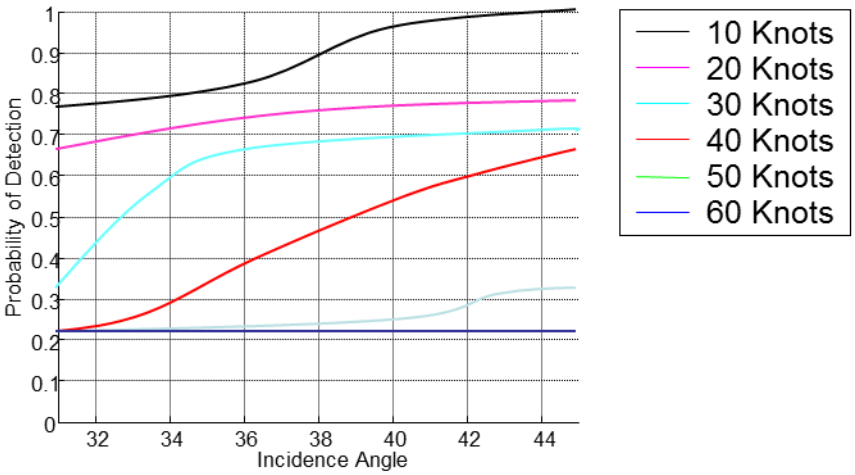

Figure 44 Probability of Detection for Large Icebergs.

6.2.5 Product summary

Table 12. Summary of properties of the iceberg product.

Product description	Product provides iceberg location information extracted from single or dual polarization SAR imagery
Satellite input data	RADARSAT-1, RADARSAT-2 (All Single pol modes and dual-pol (HH/HV) SCW, SCN, Wide, Fine), ENVISAT (Wide, IM), COSMO-SkyMed (SC Huge, SM), TerraSAR-X (single pol SC, SM), Sentinel-1 (single pol EW, IW).
Coverage	User defined
Update interval	User defined
Spatial resolution	5 – 100 m
Delivery time	3 – 24 hours
Formats	Text file, Shape file, MANICE, ICEMAR.

6.2.6 References

[1] C-CORE. An Assessment of Iceberg Detectability Using RADARSAT-2 SAE Data, C-CORE Reprot R-09-104-742 v2.0, May 2010.